JOURNAL OF PROPULSION AND POWER
Vol. 24, No. 6, November–December 2008

Repetitively Pulsed Nonequilibrium Plasmas for Magnetohydrodynamic Flow Control and Plasma-Assisted Combustion

Igor V. Adamovich,* Walter R. Lempert,† Munetake Nishihara,‡
J. William Rich,§ and Yurii G. Utkin¶
The Ohio State University, Columbus, Ohio 43210

DOI: 10.2514/1.24613

This paper demonstrates significant potential of the use of high-voltage, nanosecond pulse duration, high pulse repetition rate discharges for aerospace applications. The present results demonstrate key advantages of these discharges: 1) stability at high pressures, high flow Mach numbers, and high-energy loadings by the sustainer discharge, 2) high-energy fractions going to ionization and molecular dissociation, and 3) targeted energy addition capability provided by independent control of the reduced electric field of the direct current sustainer discharge. These unique capabilities make possible the generation of stable, volume-filling, low-temperature plasmas and their use for high-speed flow control, nonthermal flow ignition, and gasdynamic lasers. In particular, the crossed pulser-sustainer discharge was used for magnetohydrodynamic flow control in cold $M = 3$ flows, providing first evidence of cold supersonic flow deceleration by Lorentz force. The pulsed discharge (without sustainer) was used to produce plasma chemical fuel oxidation, ignition, and flameholding in premixed hydrocarbon–air flows, in a wide range of equivalence ratios and flow velocities and at low plasma temperatures, 150–300°C. Finally, the pulser-sustainer discharge was used to generate singlet oxygen in an electric discharge excited oxygen–iodine laser. Laser gain and output power are measured in the $M = 3$ supersonic cavity.

I. Introduction

OVER recent years, there has been a significant increase of interest in applications of nonequilibrium plasmas for magnetohydrodynamic (MHD) flow control [1–6], combustion augmentation [7–16], and onboard directed energy sources [17–30]. One of the key factors affecting development and scaling of these applications is the ability to efficiently generate, sustain, and control large-volume nonequilibrium plasmas in high-speed flows, at high pressures, and at high electron densities. As is well known, at these conditions, nonequilibrium plasmas are prone to ionization instability development [31]. This results in plasma constriction and formation of localized high-current, high-temperature arcs producing heating of the flow and erosion of adjoining surfaces. Several successful approaches to nonequilibrium plasma stabilization, developed in the 1970s and 1980s, include aerodynamic stabilization [32,33], as well as external ionization by an electron beam [34–36] and by high-voltage pulses [37,38]. All of these methods were originally developed for use in high-power gas lasers.

Aerodynamic stabilization prevents formation of arc filaments near discharge electrodes, using sonic injection of flow across electrode surfaces, perpendicular to the current direction. Basically, the fast flow enhances convective cooling of the near-electrode regions and dissipates incipient arc filaments. This method has been used for development of an electrically excited, gasdynamic, kilowatt range continuous wave (cw) CO laser [33], where uniform and diffuse plasma was sustained in the plenum of a supersonic nozzle at pressures of up to 10 atm.

The basis of plasma stabilization using an external ionizer is uncoupling of ionization and energy loading processes in the discharge. In this method, ionization in the flow is created by an external ionization source not coupled to the applied electric field, such as a high-energy electron beam or short pulse duration ionizing pulses. On the other hand, energy is added to the flow by an electric field set below breakdown threshold and generating electric current. This arrangement is known as a non-self-sustained electric discharge. Uncoupling of ionization and energy addition processes prevents positive feedback between the Joule heating of the plasma and the rate of ionization by electron impact, existing in self-sustained discharge plasmas [31].

Electron-beam-controlled discharges have been used in high-power CO and CO_2 lasers [34,36], as well as for singlet delta oxygen generation at high pressures in development of an electrically excited oxygen–iodine laser [19,21]. Ionization efficiency by high-energy-beam electrons (i.e., the beam energy fraction spent to generate electron–ion pairs) is very high, approaching 50% [39]. At typical beam electron energy, $\sim$100 keV, current density, $\sim$1 mA/cm^2, and penetration length, $\sim$10 cm, in atmospheric air [39], the e-beam plasma power budget is $\sim$10 W/cm^3. The electron density achieved at these conditions is $n_e \sim 10^{13}$ cm^{-3} (assuming the electron recombination rate of $\beta \sim 10^{-7}$ cm^3/s). However, in this type of discharge, great care should be exercised to shield x-ray emission and to prevent foil breaking, which may result in contamination of the electron beam apparatus as well as in severe damage of the electron gun cathode.

An alternative approach is to use two overlapping electric discharges, one producing a series of high-voltage, short pulse duration, high repetition rate ionizing pulses, and the other providing a below-breakdown sustainer voltage. In such discharges, uniform

Received 13 April 2006; revision received 21 March 2008; accepted for publication 21 March 2008.

*Associate Professor, Michael A. Chaszeyka Nonequilibrium Thermodynamics Laboratories, Department of Mechanical Engineering. Associate Fellow AIAA.

†Professor, Michael A. Chaszeyka Nonequilibrium Thermodynamics Laboratories, Department of Mechanical Engineering. Associate Fellow AIAA.

‡Postdoctoral Researcher, Michael A. Chaszeyka Nonequilibrium Thermodynamics Laboratories, Department of Mechanical Engineering. Member AIAA.

§Professor Emeritus, Michael A. Chaszeyka Nonequilibrium Thermodynamics Laboratories, Department of Mechanical Engineering. Fellow AIAA.

¶Postdoctoral Researcher, Michael A. Chaszeyka Nonequilibrium Thermodynamics Laboratories, Department of Mechanical Engineering.

ionization is produced by high-voltage, nanosecond duration pulses, which are far too short for ionization instabilities and arc filaments to develop. Basically, the pulse duration, ~10–100 ns, is much shorter than the characteristic time for the ionization instability development, $\sim 10^{-3}$–10^{-4} s [31]. Because the dc sustainer voltage is too low to produce ionization, the decaying plasma remains stable between the pulses, while the sustainer voltage draws the electric current and couples power to the plasma. This approach, first suggested and experimentally demonstrated in 1971 by Hill [37], has been used to develop a high-power, fast flow CO_2 laser with the crossed discharge volume of 27 liters [31,38]. Recent kinetic modeling calculations demonstrated that the cost of ionization and the plasma power budget in a repetitively pulsed, nanosecond pulse duration discharge in air at $P = 1$ atm, $T = 2000$ K, and $n_e = 10^{13}$ cm^{-3} can be reduced by more than 2 orders of magnitude compared to dc electric discharges [40–43]. Also, from a practical standpoint, external ionization by high-voltage pulses offers a key advantage over e-beam ionization because short duration pulse generators are much simpler to operate and maintain.

Because the rate of electron impact ionization grows exponentially with the reduced electric field E/N [31], it should be sufficiently high to achieve reasonable ionization efficiency during the pulse and thereby to reduce the plasma power budget, at least $E/N \sim 10^{-15}$ V · cm^2. This requires the pulse voltage to be in the range of a few tens of kilovolts across ~1 cm gap at $P \sim 1$ atm. Simple estimates based on the rate of ionization and electron drift velocity in air at these conditions ($k_{\text{ion}} \sim 10^{-11}$ cm^3/s, $v_{\text{dr}} \sim 10^7$ cm/s) show that, for a single-pulse energy of ~10 mJ loaded into a plasma volume of ~100 cm^3, the pulse duration should be in the range of ~10 ns at the peak electron density of $n_e \sim 10^{12}$ cm^{-3}. To increase the sustainer discharge energy loading, the pulse repetition rate should be sufficiently high to avoid complete plasma decay between the high-voltage pulses, ~100 kHz for the electron recombination rate of $\beta \sim 10^{-7}$ cm^3/s. At these conditions, the duty cycle of the pulsed discharge is extremely low, ~1/1000, and the time-averaged discharge power is ~1 kW (pulsed plasma power budget of ~10 W/cm^3). Note that high reduced electric field values during the pulses make possible efficient electronic excitation and dissociation of molecular species by electron impact, the rates of which also have strong exponential dependence on E/N [31].

A renewed interest in aerospace applications of nonequilibrium plasmas in the 1990s resulted in significant progress in studies of both e-beam-controlled and repetitively pulsed discharges. Based on encouraging modeling calculation results, predicting significant reduction of the plasma power budget in the repetitively pulsed nanosecond discharge [40–43], the use of this type of discharge was suggested for aerospace applications, such as MHD flow control and power generation. Also, it has been shown that vibrational excitation of oxygen in an e-beam-sustained, room temperature, atmospheric air plasma (using optical pumping of CO-seeded air by a cw CO laser) increases the plasma lifetime by up to 2–3 orders of magnitude [44,45]. This occurs due to a nearly complete mitigation of three-body electron attachment to O_2 molecules, which is the dominant electron removal mechanism in cold high-pressure air plasmas. Finally, it has been shown that stable, nanosecond pulse duration, high pulse repetition rate plasmas can be sustained in atmospheric pressure air [46], as well as in supersonic air flows up to $M = 3$–4 [2–5]. In both types of discharges, electron densities exceeding $n_e = 10^{12}$ cm^{-3} have been achieved at relatively modest plasma power budgets of several watts per cubic centimeter. Potential for volume scaling of nanosecond pulse generated high-pressure plasmas has been demonstrated in experiments using a fast ionization wave [7,8], where plasma was generated at $P \sim 1$ atm, across distances of up to tens of centimeters.

The present paper reviews recent and ongoing nanosecond pulse plasma experiments at The Ohio State University, targeted for the following aerospace applications: cold plasma/MHD flow control (Sec. II), nonequilibrium plasma-assisted combustion (Sec. III), and development of an electrically excited oxygen–iodine laser (Sec. IV).

II. Low-Temperature Plasma/Magnetohydrodynamics Flow Control

Over the last few years, numerous theoretical system studies and modeling calculations analyses of low-temperature magnetohydrodynamics for supersonic flow control and power generation have been complemented by experimental results. Repetitively pulsed nanosecond discharge has been used at Princeton University to demonstrate feasibility of MHD power extraction [4], as well as Lorentz force acceleration of a constricted discharge filament sustained in the boundary layer of a cold $M = 3$ air flow [5]. The latter result suggests the possibility of boundary-layer acceleration by momentum transfer from the accelerated filament to the neutral flow due to collisions between the charged species and the neutral species, (the "snowplow" effect [5]). Nonequilibrium MHD flow experiments at Wright–Patterson Air Force Base showed that a near-surface dc glow discharge combined with the magnetic field can be used to control surface pressure on a model in a $M = 5$ air flow [6]. Finally, experiments at The Ohio State University showed that retarding Lorentz force produces significant density fluctuation increase in a supersonic boundary layer, as well as core flow deceleration in low-temperature $M = 3$ nitrogen and air flows [1–3]. In these recent experiments, ionization in cold supersonic flows (stagnation temperature $T_0 = 300$ K) was generated by a high-voltage, short pulse duration, high pulse repetition rate discharge.

A. Experimental

The experiments have been conducted at a supersonic nonequilibrium plasma/MHD wind tunnel [1–3], generating stable and diffuse supersonic nonequilibrium plasmas flows at $M = 3$–4 in a uniform magnetic field up to $B = 2$ T, and operating at steady state. The schematic of the nozzle and an MHD test section is shown in Fig. 1. A contoured supersonic nozzle made of transparent acrylic plastic is connected to a 2×4 cm rectangular cross section test section, 12 cm long with an angle step diffuser. The nozzle/test section/diffuser assembly is attached to a vacuum system, connected to a 1200 ft^3 dump tank, pumped out by an Allis-Chalmers 1300 cfm rotary vane vacuum pump. The nozzle assembly is equipped with

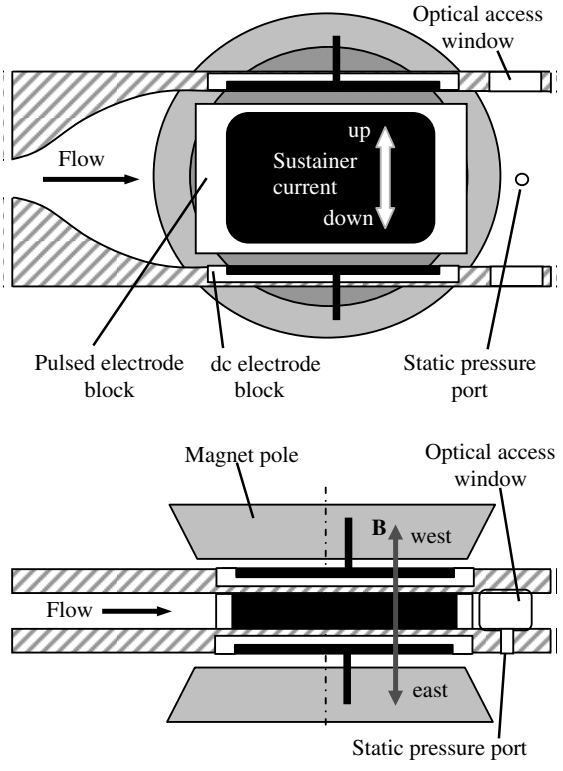

Fig. 1 Schematic of a supersonic nozzle and MHD test section.

pressure taps measuring plenum pressure as well as static pressures at the beginning and the end of the test section. The nozzle throat dimensions are 20×9.5 mm, which gives a mass flow rate through the test section of $\dot{m} = 15$ g/s at $P_0 = 1/3$ atm.

Two 5-cm-long rectangular electrode blocks are flush mounted in the side test section walls (see Fig. 1). Each electrode block, made of mica ceramic, incorporates a single copper plate electrode. The electrode edges are rounded using a Rogowski profile [47] to achieve a more uniform electric field distribution between the electrodes. Each electrode is separated from the flow by a 2-mm-thick ceramic layer. Ionization in the test section is produced using a Chemical Physics Technologies custom-designed, high-voltage (up to 20 kV peak), short pulse duration (~10–20 ns), high repetition rate (up to 50 kHz), pulsed plasma generator. During the pulser operation, pulse voltage and current are measured using a Tektronix P6015A high-voltage probe, a custom-made, low-capacitance resistive current probe, and a LeCroy Wavepro 7100A digital oscilloscope.

Transverse dc electrical current (sustainer current) in the supersonic flow, ionized by the repetitively pulsed discharge, is sustained by applying a dc field, two 5×2 cm dc electrode blocks flush mounted in the top and bottom nozzle walls 4 cm apart, perpendicular both to the flow velocity and to the magnetic field direction, as shown in Fig. 1. The dc electrode blocks are made of boron nitride ceramic, with continuous copper electrodes, 45 mm long each. The transverse dc field, which is far too low to produce additional ionization in the flow, is needed to sustain transverse (Faraday) current. The field is applied using a DEL 2 kV/3 A power supply (Del High Voltage Corp.) operated in a voltage-stabilized mode, with a 0.5–1.0 kW ballast. Two inductors, 1 mH each, are placed in the dc circuit in series with both dc electrodes to attenuate high amplitude voltage and current pulses propagation into the dc circuit. Current in the dc sustainer circuit is measured using a Tektronix AM503B current probe.

Optical access to the flow is provided using two $1 \times 1/2$ in. glass windows in the top and bottom walls of the test section (see Fig. 1). The MHD effect on a supersonic ionized boundary layer was studied using laser differential interferometry (LDI) diagnostics [48]. Briefly, a He–Ne laser beam is split into two beams using a Wollaston prism (see Fig. 2) and is sent through two different regions of the supersonic flow, with the reference beam passing through the flow along the centerline and the probe beam passing through the boundary layer (see Fig. 2). The phase shift between the two beams is proportional to the average density difference along the two beam paths. Fourier transform of the beam interference signal yields the boundary-layer density fluctuation spectrum. The laser beam diameters, which limit the spatial resolution of the LDI signal, are approximately 2 mm each. The location of the probe beam can be controlled by rotating the prism.

Figure 3 shows a photograph of the $M = 3$ test section. The entire nozzle/test section/diffuser assembly is placed between the poles of a GMW water-cooled electromagnet, as shown in Figs. 1 and 2. For the distance between the 15-cm-diam poles of 6 cm, the magnetic field at maximum current through the magnet coils of 140 A is $B = 1.8$ T. Both the magnet and the dc power supply were operated continuously. No breakdown was produced in the test section and no current was measured in the dc circuit until the high-voltage pulse train was initiated. After the gas flow was started and test section pressure reached steady state, the pulser was turned on. After the high-voltage pulse train stopped, the discharge always extinguished. Time-dependent static pressure at the end of the test section was monitored by a high accuracy Omega PX811-005GAV pressure transducer, at a sampling rate of 67 Hz (time resolution of 15 ms). The pressure tap used for these measurements is located in the side wall of the test section, 3 cm downstream of the dc electrodes, as shown in Figs. 1 and 3. The pressure transducer was placed at a distance of about 2 m from the test section, which was sufficient to nearly completely remove electromagnetic interference from the pulsed discharge.

LDI and static pressure measurements have been performed for both accelerating and decelerating Lorentz force directions. In both these cases, Lorentz force can be generated by two possible combinations of the transverse B field and the transverse dc electric field directions. Control runs in a cold supersonic flow without plasmas and in an ionized flow without dc electric field applied, that is, when the time-averaged Lorentz force is zero, have also been conducted. The purpose of this approach was to isolate the MHD effect, which should depend on the Lorentz force direction, from the polarity-independent effect of Joule heat. The experiments were conducted in nitrogen and dry air.

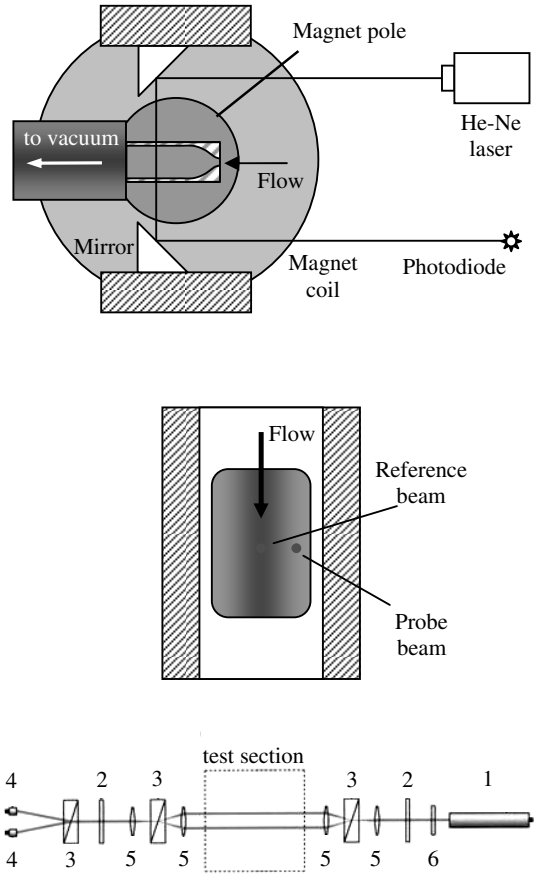

Fig. 2 Layout and schematic of the LDI diagnostics.

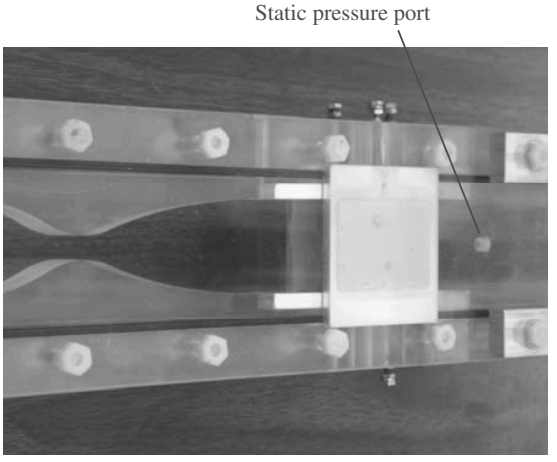

Fig. 3 Photograph of a $M = 3$ test section.

B. Results and Discussion

Figure 4 shows a photograph of a crossed pulser-sustainer discharge in a $M = 4$ air flow at $P_0 = 1$ atm and $B = 1.5$ T, at a pulse repetition rate of $\nu = 40$ kHz. Visual observation of the discharge showed the plasma to be stable and uniform, without "hot spots" appearing in the test section corners. Figure 5 shows typical single-pulse voltage and current oscillograms in a $M = 3$ nitrogen flow at $P_0 = 250$ torr, $P_{\text{test}} = 8.4$ torr, respectively, at the magnetic field of $B = 1.5$ T. The peak voltage and current at these conditions are 13.2 kV and 31.2 A, respectively, with pulse duration [full width at half-maximum (FWHM)] of approximately 30 ns. The pulse energy coupled to the flow, calculated from the current and voltage traces at these conditions, was in the range of 1–2 mJ. Figure 6 shows several voltage pulses generated at the pulse repetition rate of $\nu = 40$ kHz, at the same flow conditions. From Fig. 6, it can be seen that, at this pulse repetition rate, the voltage duty cycle is extremely low, $\sim$30 ns/25 μs $\sim 1/1000$. As discussed in Sec. I, the high reduced electric field during the pulses, $E/N \sim 7 \cdot 10^{-15}$ V $\cdot$ cm^2 (70 Td), makes possible efficient ionization by electron impact. On the other hand, the short pulse duration and the low duty cycle greatly improve the plasma stability.

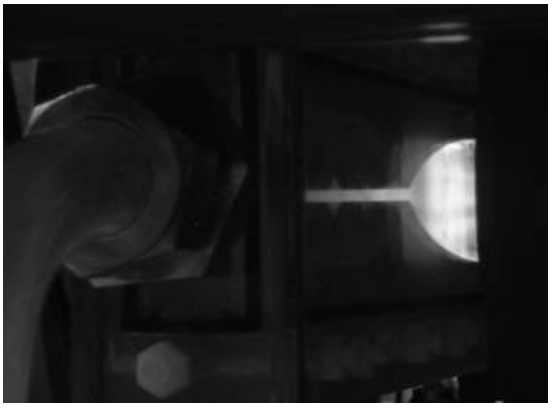

Fig. 4 Photograph of a pulsed discharge in a $M = 3$ air flow. $P_0 = 760$ torr, $P_{\text{test}} = 10$ torr, pulse repetition rate 40 kHz, $B = 1.5$ T. The discharge is seen at an oblique angle, looking in the direction of the flow.

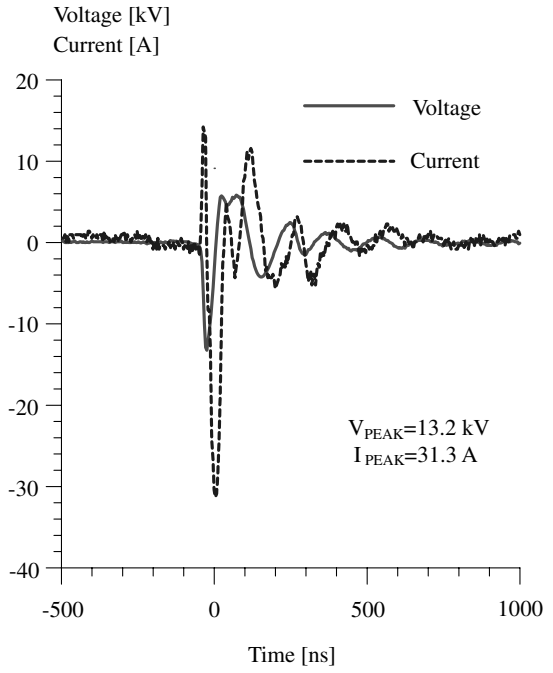

Fig. 5 Single-pulse voltage and current oscillograms in a $M = 3$ nitrogen flow at $P_0 = 250$ torr, $P_{\text{test}} = 8.4$ torr, and $B = 1.5$ T.

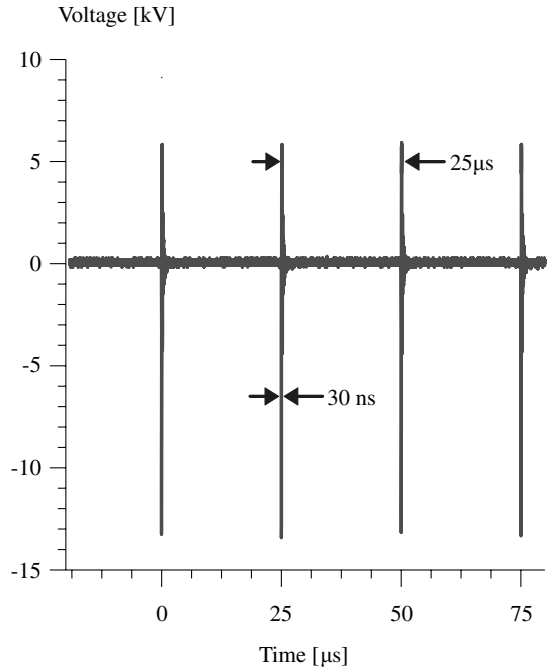

Fig. 6 Repetitively pulsed voltage oscillogram in a $M = 3$ nitrogen flow at $P_0 = 250$ torr, $P_{\text{test}} = 8.4$ torr, and $B = 1.5$ T. Pulse repetition rate is $\nu = 40$ kHz.

Figure 7 shows dc sustainer current oscillograms in a pulse-ionized $M = 3$ nitrogen flow at the conditions of Figs. 5 and 6. In Fig. 7, current traces are shown for dc power supply voltage of $U_{\text{PS}} = 2$ kV and ballast resistor of $R = 0.5$ kΩ, for two different electric field polarities. The voltage between the dc electrodes is $U = U_{\text{PS}} - IR$, where I is the sustainer current. In this figure, the current pulses produced during the high-voltage pulses are not resolved. It can be seen that, after each ionizing pulse, the sustainer current reaches approximately $I = 2$ A, with the subsequent falloff in a decaying plasma between the pulses, to a minimum value of

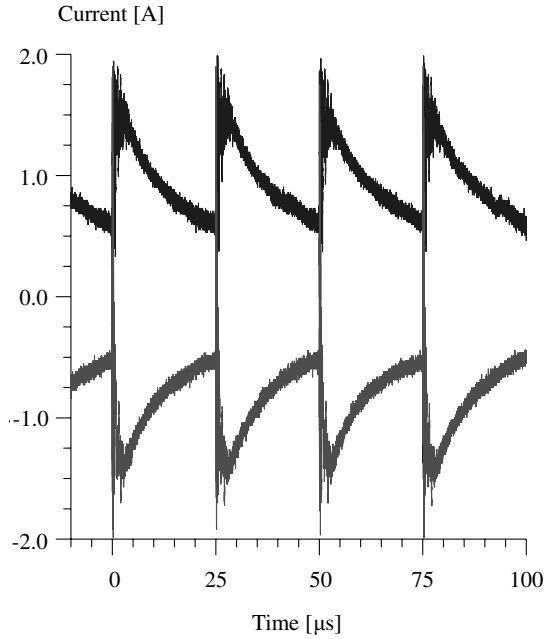

Fig. 7 Sustainer (Faraday) current traces for two different transverse dc electric field polarities, at the conditions of Figs. 5 and 6. $U_{\text{PS}} = 2$ kV, $R = 0.5$ kΩ. Time-averaged currents are 0.95 A (top curve) and 0.86 A (bottom curve).

about $I = 0.5$ A. Note that the plasma does not fully decay between the pulses. The time-averaged currents at these conditions are close, $\langle I \rangle = 0.95$ and 0.86 A. In dry air, at the same flow and plasma conditions, the time-averaged current was up to $\langle I \rangle = 1.0$–1.3 A. In the entire range of experimental conditions, the discharge plasma was uniform and stable, filling the entire volume of the flow in the MHD section. The magnetic field helped stabilize the discharge, dissipating sustainer current oscillations occurring in the absence of the magnetic field. This behavior suggests that the supersonic plasma flow in the MHD section can be analyzed using a quasi-one-dimensional MHD flow model.

The time-averaged dc discharge power added to the flow at these conditions is approximately 1.1–1.5 kW, which, in case of instant thermalization, would result in the estimated flow temperature rise of about $\Delta T = 70$–100 K, from the baseline core flow temperature at $M = 2.9$ of $T = 110$ K. However, at the reduced electric field in the sustainer discharge of $E/N = 5$–$6 \cdot 10^{-16}$ V $\cdot$ cm^2 (based on the initial core flow temperature), about 90% of the discharge power in nitrogen and air goes to vibrational excitation of nitrogen [31], the vibrational relaxation rate of which is extremely slow [49]. Basically, the slow vibrational relaxation rate locks up the energy stored in nitrogen vibrations and makes the supersonic flow essentially frozen. Assuming that the rest of the discharge power ($\sim$10%) thermalizes, the resultant inviscid core flow temperature rise would be significantly lower, only up to $\sim$10 K. Note that energy addition to the flow by the repetitively pulsed discharge, based on the measured single-pulse energy, 1–2 mJ, is insignificant: 40–80 W at the pulse repetition rate of $\nu = 40$ kHz, or only a few percent of the energy loading by the dc sustainer discharge.

Figure 8 shows current voltage characteristics of the MHD sustainer discharge in $M = 3$ nitrogen flows at $P_0 = 250$ torr and $P_{\text{test}} = 7.5$ torr. It can be seen that, at low voltages, the sustainer current remains very low and nearly independent of the applied voltage, whereas, at high voltages, the current exhibits linear voltage dependence, as expected for the constant conductivity plasma. Similar results were obtained in $M = 3$, $P_0 = 250$ torr dry air flows. The cathode voltage falls for different B fields were determined from the x-axis intercept of the linear slope of the current voltage characteristics, as shown in Fig. 8. In the absence of magnetic field, the cathode falls in nitrogen and in air are $U_c = 260 \pm 50$ V and $U_c = 350 \pm 50$ V, which is close to the normal self-sustained glow discharge cathode fall, 208 V in nitrogen and 370 V in air (both for copper cathode) [31]. These measurements show that, both in nitrogen and air, the cathode fall increases with the magnetic field, up to $U_c = 500 \pm 50$ V and $U_c = 520 \pm 50$ V at $B = 1.5$ T in nitrogen and air, respectively, (e.g., see Fig. 8). This result is consistent with the electrical breakdown theory in crossed electric and magnetic fields [50] and with experimental measurements of breakdown voltages in crossed fields in nitrogen [51], both of which predict breakdown voltage to increase with the magnetic field because of the Hall effect.

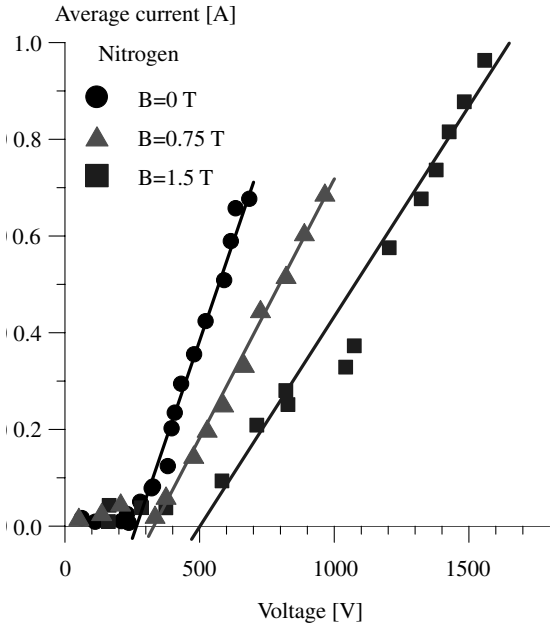

Fig. 8 Current voltage characteristics of the sustainer discharge in $M = 3$ flows of nitrogen at different values of magnetic field. $P_0 = 250$ torr, $P_{\text{test}} = 7.5$ torr, pulse repetition rate 40 kHz.

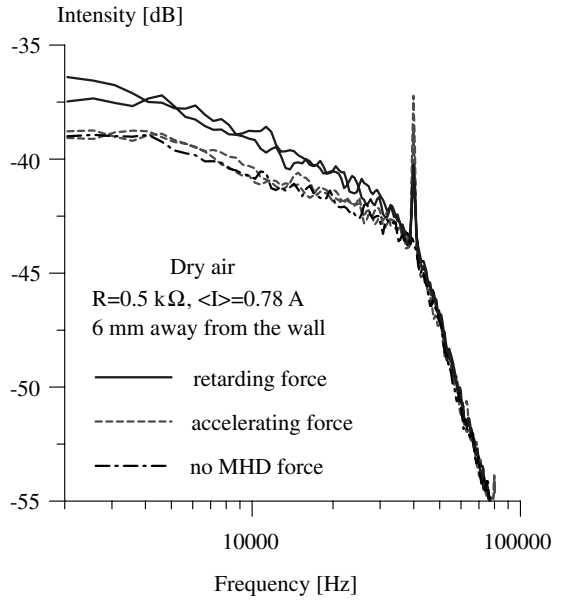

Fig. 9 LDI spectra in a crossed discharge in a $M = 3$ flow of dry air at $P_0 = 250$ torr for different Lorentz force directions. Both accelerating and retarding j × B force directions are created by two different combinations of j and B vectors.

Figure 9 shows the LDI spectra in $M = 3$ dry air flows at the plenum pressure of $P_0 = 250$ torr, magnetic field $B = 1.5$ T, sustainer voltage $U_{\text{PS}} = 2$ kV, and the LDI probe beam placed 6 mm from the wall, that is, near the outer edge of the boundary layer [2]. In [2], boundary-layer thickness in $M = 3$ flows seeded with acetone vapor was determined by Nd:YAG laser sheet scattering flow visualization. The spectra are shown for the ballast resistor of $R = 0.5$ kΩ (time-averaged MHD current of $\langle I \rangle = 0.78$ A), both for accelerating and retarding Lorentz force directions. The four spectra shown correspond to four possible combinations of the MHD current and the magnetic field vectors **j** and **B**, two of which correspond to the accelerating Lorentz force and the other two to the retarding Lorentz force, $\mathbf{F} = \mathbf{j} \times \mathbf{B}$. This has been done by switching the dc power supply polarity and/or the magnet power supply polarity. One can see that both retarding force combinations produce significantly higher density fluctuation intensities in the frequency range of 2–40 kHz compared with both accelerating force combinations, up to 2 dB (about 25%). Figure 9 also shows LDI spectra measured with the pulsed power supply operating, but with the dc sustainer voltage turned off, that is, when there was no MHD force applied to the flow. It can be seen that, at these conditions, the density fluctuation spectra are very close to the spectra measured with the accelerating MHD force applied. The LDI spectra measured in nitrogen and air flows without plasmas (i.e., with both power supplies turned off) are nearly identical to the spectra with only the pulser operating. These results show that, in both cases, the effect on the density fluctuations is detected only when the retarding MHD force is applied to the flow, as well as provide strong evidence that the observed effect is indeed due to Lorentz force, not Joule heating of the flow.

Figure 10 shows normalized test section static pressure traces measured in $M = 3$ dry air flows at the conditions of Figs. 5–7, with and without Lorentz force applied. The baseline static pressure, measured using the pressure tap downstream of the MHD section, shown in Figs. 1 and 3, was $P = 8.4$ torr, which corresponds to the Mach number of $M = 2.9$. Turning the pulser on in the presence of

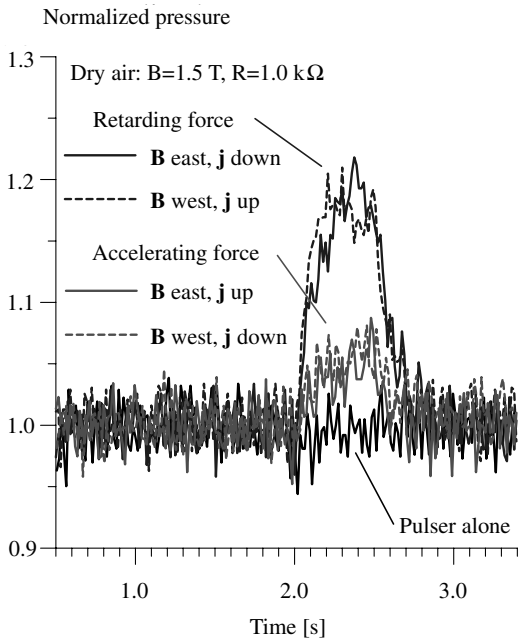

Fig. 10 Normalized static pressure traces in $M = 3$ dry air flows at $P_0 = 250$ torr, $P_{\text{test}} = 8.7$ torr, $B = 1.5$ T, $\nu = 40$ kHz. $U_{\text{PS}} = 2$ kV, $R = 1.0$ kΩ. Lorentz force is applied for 0.5 s duration.

the magnetic field, without applying transverse dc electric field, that is, generating ionization in the test section without applying Lorentz force, did not produce detectable static pressure rise (see Fig. 10). This suggests that Joule heating generated by the pulser is negligibly small. In addition to this baseline pressure trace, four pressure traces plotted in Fig. 10 correspond to four possible combinations of the transverse current and the magnetic field vector directions, shown schematically in Fig. 1. Two of these combinations result in accelerating Lorenz force $\mathbf{j} \times \mathbf{B}$, whereas two others produce retarding Lorentz force. In each one of these runs, the pulser was turned on for 0.5 s.

From Fig. 10, it can be seen that, in all four cases, generating transverse current in the MHD section results in the static pressure increase. This behavior points to Joule heating of the flow by the transverse dc discharge as one of the sources of the pressure rise. However, for both **j** and **B** vector combinations corresponding to the accelerating Lorentz force, the pressure rise of 5–7% is noticeably lower than for both retarding Lorentz force combinations, 18–21%. The dependence of the static pressure rise on the Lorentz force polarity suggests that the pressure and the flow Mach number may also be affected by the MHD force interaction. Similar results were obtained in a nitrogen flow at the same flow conditions. Control runs in nitrogen and dry air have been made with the magnetic field turned off, at $B = 0$. In the absence of the magnetic filed, sustainer discharge voltage had to be reduced to $U_{\text{PS}} = 1$ kV to prevent sustainer current oscillations and instability development. As a result, the discharge power decreased from about 1.5 kW (see Fig. 7) to about 0.5 kW. The sustainer current at these conditions, $\langle I \rangle = 0.60$–0.65 A, was comparable to the current at $B = 1.5$ T, $\langle I \rangle = 0.86$–0.95 A (see Fig. 7). In this case, no pressure difference was detected between two dc discharge polarities, the pressure rise being about 3% in both cases. This provides additional evidence that the static pressure difference detected at $B = 1.5$ T and shown in Fig. 10 is indeed due to the Lorentz force interaction.

The results of static pressure measurements in the presence of the Lorentz force and Joule heat have been analyzed using quasi-one-dimensional MHD flow equations [52]. Integrating these equations [3] gives the following expressions for the pressure rise difference between the retarding and the accelerating Lorentz force cases, $\Delta p_R - \Delta p_A$,

$$\Delta p_R - \Delta p_A \cong 2 \cdot \frac{(\gamma - 1)M^2 + 1}{M^2 - 1} \cdot jBL \tag{1}$$

and for the effective Joule heating factor α (discharge energy fraction spent on heating the flow),

$$\alpha \cong \frac{\Delta p_A + \Delta p_R}{2} \frac{M^2 - 1}{(\gamma - 1)M} \frac{a}{jEL} \tag{2}$$

In Eqs. (1) and (2), E is the transverse electric field, j is the transverse current density, $L = 5$ cm is the MHD section length, and a is the speed of sound. For the baseline conditions, $p = 8.5$ torr, $T = 110$ K, $M = 2.9$, $\gamma = 1.4$, $I = 1.0$ A, and $U = 1.5$ kV, Eq. (1) gives $(\Delta p_R - \Delta p_A)/p \approx 0.08$. This pressure difference is consistent with the experimental results shown in Fig. 10. Using Eq. (2), with the results of Fig. 10, the effective Joule heating factor is $\alpha \approx 0.11 \pm 0.02$, which is in good agreement with the results of the Boltzmann equation solution [53], $\alpha = 0.09$ in nitrogen at the reduced electric field of $E/N = 6 \cdot 10^{-16}$ V · cm^2 and $\alpha = 0.10$ in air at $E/N = 5 \cdot 10^{-16}$ V · cm^2. At these conditions, the effective MHD loading parameter (the ratio of the effective Joule heating and the Lorentz force work),

$$K = \frac{\alpha \cdot jE}{jBu} = \frac{\alpha \cdot E}{Bu} \tag{3}$$

is $K \approx 4$. Therefore, this analysis suggests that the observed static pressure difference between the accelerating and the retarding Lorentz force runs is indeed due to the MHD force interaction, superimposed on the pressure rise due to Joule heating of the flow in the discharge.

Note that the characteristic time for the static pressure change due to both MHD forcing and Joule heating of the supersonic core flow measured in the present experiments is ~0.2 s (see Fig. 10), which is much longer than the flow residence time in the discharge section, ~100 μs. Varying the length of the $\frac{1}{4}$ in. line, connecting the wall static pressure tap and the pressure transducer from 2 to 4 m, showed that it is, in fact, the long line that controls the pressure measurement system response time. In the present experiments, removing the line and placing the pressure transducer near the static pressure tap was not feasible because of strong electromagnetic interference of the pulsed discharge with the transducer.

Figure 11 compares static pressure measurements with the results of numerical integration of quasi-one-dimensional MHD flow equations [3,52], for three different values of the effective Joule heating parameter, $\alpha = 0$ (no Joule heating), $\alpha = 0.05$, and $\alpha = 0.10$. In Fig. 11, positive values of the current correspond to the

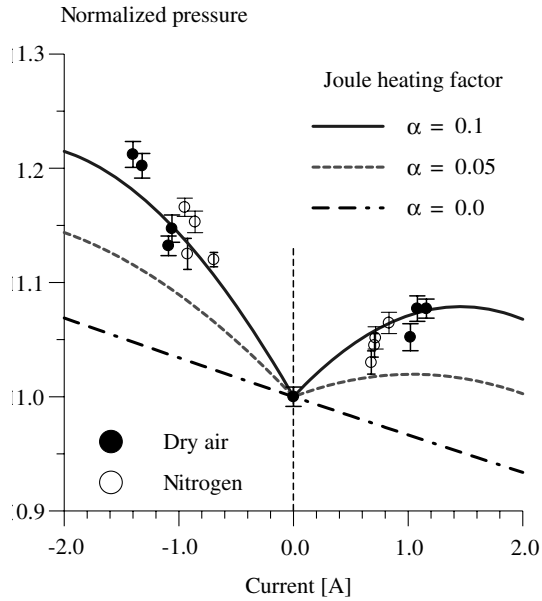

Fig. 11 Experimental and calculated normalized pressure in nitrogen and air at $P_0 = 250$ torr, $U_{\text{PS}} = 2$ kV, and $R = 0.5$ kΩ. Calculation results are shown for different values of the Joule heating factor α.

accelerating Lorentz force. It can be seen that the results of calculations for $\alpha = 0.10$ are in good agreement with the experimental data. Figure 11 also illustrates how Joule heating superimposed over Lorentz force affects the static pressure change. Specifically, whereas the calculations at $\alpha = 0$ (no Joule heating) predict static pressure reduction (i.e., Mach number increase) for the accelerating MHD force and static pressure increase (i.e., Mach number reduction) for the retarding MHD force, Joule heating results in static pressure rise in both cases. However, the predicted static pressure increase is always higher for the retarding MHD force, which was indeed observed in the present experiments. From Fig. 11, flipping the Lorentz force direction from accelerating to retarding force at $\alpha = 0.10$ and $I = 1.0$ A results in a static pressure rise, which corresponds to a Mach number change from $M = 2.77$–2.64 ($\Delta M = -0.13$).

Figure 12 summarizes the results for the normalized static pressure difference for two Lorentz force directions, $(\Delta p_R - \Delta p_A)/p$, as a function of the transverse sustainer current obtained in $M = 3$ nitrogen and dry air flows. It can be seen that the measured relative pressure change increases nearly proportional to the current and reaches about 13% at $\langle I \rangle = 1.2$–1.3 A. This behavior is in good agreement with the prediction of quasi-1-D MHD theory, Eq. (1). We conclude that the dependence of the static pressure change on the Lorentz force magnitude and polarity, which is consistent with the results of the quasi-one-dimensional MHD flow analysis, conclusively demonstrates supersonic flow deceleration by the Lorentz force. We emphasize that this effect could be detected only because the Joule heating factor in nitrogen and in dry air is small, $\alpha \sim 0.1$. If this were not the case, at low electrical conductivities achieved at the present experimental conditions, the MHD effect would be overshadowed by Joule heating of the flow.

Demonstration of net MHD acceleration of the flow, when the Mach number increase and the static pressure is reduced, would require reducing Joule heating while keeping the Lorentz force the same. This is equivalent to reducing the loading parameter, determined by Eq. (3), to $K \sim 1$. Because, at the present experimental conditions, the loading parameter is $K \sim 4$ (at $\alpha \sim 0.1$), this suggests that net flow acceleration could be achieved if either the effective Joule heating factor or transverse electric field are reduced by a factor of 4, down to $\alpha = 0.025$ or $E = 100$ V/cm, respectively, or if the magnetic field is increased by a factor of 4, up to $B = 6$ T. Note that keeping the Lorentz force the same, while reducing the electric field, can be done only if the effective electrical conductivity of the flow σ is increased, so that the same transverse current $j \sim \sigma E$ would be sustained at a lower transverse electric field.

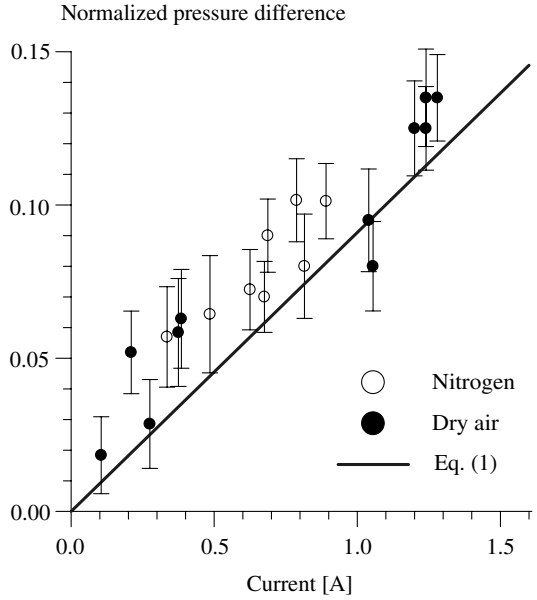

Fig. 12 Experimental and calculated normalized pressure difference $(\Delta p_R - \Delta p_A)/p$ as a function of the MHD current.

Therefore, reducing the electric field by a factor of 4 would require quadrupling the conductivity by either increasing the pulse peak voltage or the pulse repetition rate. Experiments at higher pulse voltage, ~40 kV, and pulse repetition rate, 100 kHz, are currently underway.

III. Nonequilibrium Plasma-Assisted Combustion

Recent experiments on ignition of premixed hydrocarbon–air flows, using transverse low-temperature RF discharge plasma and repetitively pulsed nanosecond discharge plasma, demonstrated that large-volume flow ignition can be produced at plasma temperatures significantly lower than the autoignition temperature by 300–400°C [12–14]. Experiments on ignition of nonflowing preheated hydrogen–air and hydrocarbon–air mixtures by a single-pulse fast ionization wave discharge [7,8,10] demonstrated that ignition delay time can be substantially reduced compared with autoignition at the same temperature. Finally, repetitively pulsed nanosecond duration plasma has been used for flame stabilization [9,15,16]. These results are consistent with the experiments on photochemical ignition of hydrogen–air and methane–air mixtures [54,55], which suggest that nonthermal ignition can be achieved by using a pulsed excimer laser to generate active radical species in a combustible mixture. These recent advances contribute to developing an energy-efficient nonequilibrium plasma ignition and flame stabilization method, which could be used both at low pressures and high flow velocities, as well as in fuel lean mixtures, that is, when common ignition approaches are ineffective. As discussed in Sec. I, the high-voltage, short pulse duration, high pulse repetition rate discharge both greatly improves the plasma stability and results in efficient ionization, electronic excitation, and dissociation of molecular species by electron impact, the rates of which have strong exponential dependence on E/N [31]. This may result in generation of large amounts of active radical species at a relatively low plasma power budget, which could significantly influence ignition and combustion kinetics.

A. Experimental

The experiments have been conducted at a high-speed flow plasma combustion facility [12–14]. A premixed hydrocarbon–air flow enters the 5×1 cm rectangular cross section, 30-cm-long test section through a 50 ft long, 1-in.-diam corrugated gas supply line. The facility can use either room air or cylinder air. A spring-loaded shutoff valve and a flash arrester installed in the $\frac{1}{4}$-in.-diam fuel supply line enable quick flow shutoff and prevent the flame propagation into the fuel cylinder. Downstream of the test section, the flow is diluted with atmospheric air through a vent valve to prevent further combustion in the vacuum system. The facility uses the same vacuum tank and vacuum pump as described in Sec. II.A. The test section static pressure ranges from 40 torr to 0.5 atm. The mass flow rate through the test section can be varied from below 1 to 12 g/s. The test section pressure and the mass flow rate can be varied independently. This makes the experimental facility suitable for combustion studies, both in high-speed, low-pressure and in low-speed, intermediate pressure flows.

The test section, made of steel, is shown in greater detail in Fig. 13. The flow enters the rectangular cross section test section through a $\frac{1}{2}$-in.-long ceramic honeycomb flow straightener (300 holes/in.^{2}), which also serves as an additional flashback arrester, and passes between two electrode blocks. Each of the two 5×4 cm rectangular electrode blocks are manufactured of acrylic plastic and are flush mounted in the top and bottom test section walls, with copper electrode plates placed into recesses machined in the electrode blocks, as shown in Fig. 13. The electrodes are rounded at the edges to prevent high electric field concentration and hot spot formation in the plasma near the edges. The electrodes are separated from the flow by $\frac{1}{16}$-in.-thick macor ceramic plates. The copper electrode leads are soldered to the electrode plates and insulated from the grounded test section by acrylic plastic cylindrical sleeves. Two plastic inserts are also flush mounted in the side walls of the test section, as shown in

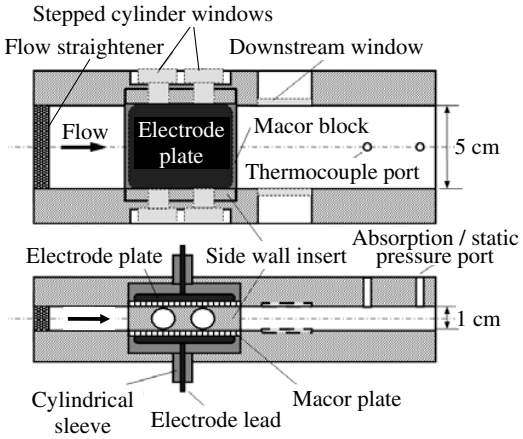

Fig. 13 Schematic of the plasma-assisted combustion test section.

Fig. 13, to prevent the discharge between the high-voltage electrode and the grounded test section. Four stepped cylinder BK-7 glass windows are used to provide optical access to the discharge region through 10-mm-diam circular holes machined in the test section and in the side wall inserts. The main objective of this design was to confine the discharge plasma to the area between the ceramic plates on top and bottom and between the side wall inserts, without extending to the steel walls of the test section. Striking a discharge between the high-voltage electrode and a test section wall would result in arc filament and hot spot formation in the plasma. Two additional rectangular windows, also made of BK-7 glass, are located approximately 1 cm downstream of the discharge region (see Fig. 13). Finally, a static pressure/flow sampling port is placed at the downstream end of the test section. The electrodes are connected to a Chemical Physics Technologies pulsed plasma generator described in Sec. II.A. In the present experiments, the top electrode is connected to the high-voltage output of the pulser, and the bottom electrode is grounded. During the pulser operation, current and voltage in the pulsed discharge are measured using a Tektronix P6015A high-voltage probe and a low-capacitance resistive current probe. The current and voltage waveforms are analyzed by a 1 GHz LeCroy WavePro 7100A digital oscilloscope.

Optical diagnostics used in the present work included visible emission spectroscopy and Fourier transform infrared (FTIR) absorption spectroscopy. For the emission spectroscopy measurements, we used an Optical Multichannel Analyzer (OMA) with a Princeton Instruments intensified charge-coupled device (CCD) array camera and a Spectra Physics 0.5 m monochromator with a 1200 g/mm grating. The emission spectra of the plasma were taken through one of the circular windows, while emission spectra of the flame were taken through the rectangular window downstream of the discharge region. The FTIR absorption spectra of the combustion products were taken with a Biorad 175C dynamic alignment FTIR spectrometer with liquid nitrogen cooled InSb detector spectrometer. For this, the flow was sampled through the static pressure/flow sampling port at the downstream end of the test section into a 17.5-cm-long cylindrical glass absorption cell with two CaF_2 windows placed into an absorption compartment of the Fourier transform (FT) spectrometer. The absorption spectra are measured at a resolution of 0.5 cm^{-1} using an internal source (globar) of the FT spectrometer. All measurements have been conducted using room air–fuel mixtures.

B. Results and Discussion

The experiments have been conducted in methane–air and ethylene–air and mixtures, at test section pressures of $P=$ 50–200 torr, mass flow rates of $\dot{m} = 0.8$–1.6 g/s, and pulse repetition rates of $\nu = 10$–50 kHz. At these conditions, pulse peak voltage and current were approximately 9 kV and 40 A, respectively, with the voltage pulse width at half-maximum of about 50 ns. At the baseline conditions, that is, test section pressure and temperature of $P = 0.1$ atm, $T = 300$ K, the peak reduced electric field in the plasma generated by the pulse is $E/N \sim 40 \cdot 10^{-16}$ V · cm^2. This upper-bound estimate does not take into account the voltage fall across the plasma sheaths and the ceramic plates covering the electrodes. The pulse energy coupled to the flow, calculated from the voltage and current waveforms at these conditions, was 6 mJ. At the pulse repetition rate of $\nu = 40$ kHz, the duty cycle is extremely low, $\sim 1/500$. As discussed in Sec. I, high E/N values during the pulses makes possible efficient electronic excitation and dissociation of molecular species by electron impact. To prevent overheating of the pulsed electrode blocks, in the present experiment, the pulser run time was limited to 1 s. This time was sufficient to take visible emission spectra of the plasma and to draw a sample of the flow into the absorption cell of the FTIR. In the entire range of experimental conditions, the repetitively pulsed plasma appeared diffuse and stable. At the conditions when ignition was achieved in the test section, a long flame originated in the plasma and extended downstream through the test section, visible through the rectangular optical access window (see Fig. 14).

Visible emission spectra of the plasma (partially rotationally resolved $0 \rightarrow 2$ band of the $N_2(C^3\Pi_u \rightarrow B^3\Pi_g)$ second positive band system) have been used to infer the flow rotational temperature. For this, synthetic spectrum has been used, with the accurate nitrogen molecular constants [56], rotational-like intensities [57], and experimentally measured slit function of the spectrometer. Figure 15 shows the experimental and the synthetic nitrogen emission spectra in stoichiometric ethylene–air mixture at $P = 70$ torr, $\dot{m} = 0.8$ g/s, and $\nu = 40$ kHz. This method of temperature inference requires calibration, because the radiative lifetime of the $N_2(C^3\Pi_u, v = 0)$ state, 38 ns [58], is comparable to the rotational relaxation time at the present conditions. Calibration was done by comparing the synthetic and the experimental spectra measured in air preheated by an in-line flow heater up to $T = 20$–180°C, at $P = 70$ torr and $\dot{m} = 1.0$ g/s. In these measurements, pulse repetition rate and time-averaged discharge power were low, $\nu = 5$ kHz and 6 mJ · 5 kHz ≈ 30 W, respectively. At these conditions, the flow temperature rise in the plasma is small, $\sim$30°C. Figure 16 compares plasma temperatures inferred from the nitrogen emission spectra with thermocouple measurements in the absence of the plasma, at the same location. It can be seen that the agreement between the two temperatures is very good, within the uncertainty of the temperature inference, ± 25 K.

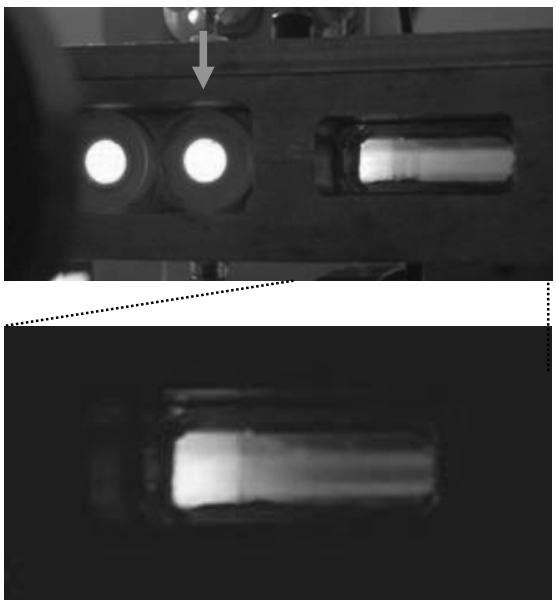

Fig. 14 Photographs of the repetitively pulsed discharge plasma (visible through the circular windows in the test section, top) and of the flame extending downstream of the discharge section (bottom). Stoichiometric ethylene–air flow, $P = 70$ torr, mass flow rate 0.8 g/s, pulse repetition rate 40 kHz. Flow is left to right. Arrow shows the window used for the plasma temperature measurements.

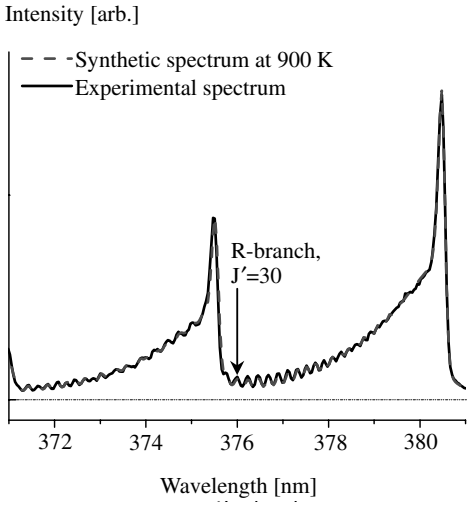

Fig. 15 Experimental and synthetic N_2 second positive band system spectra. Stoichiometric ethylene–air mixture, $P = 70$ torr, mass flow rate 0.8 g/s, pulse repetition rate 40 kHz, with flame observed in the test section.

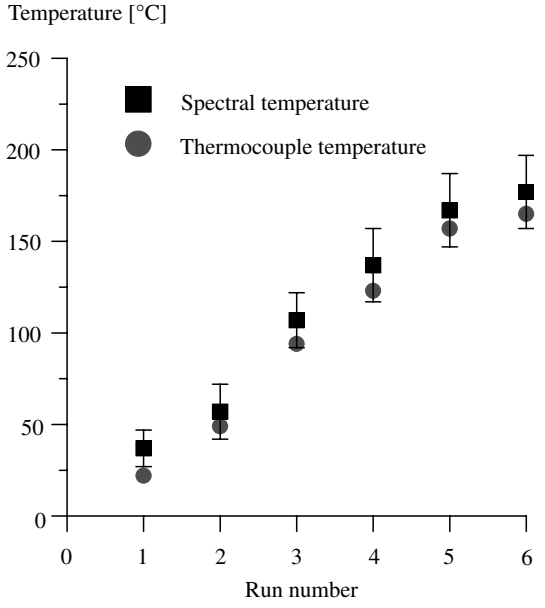

Fig. 16 Comparison of preheated flow temperatures inferred from N_2 second positive spectra at a low discharge power with thermocouple measurements. Air, $P = 70$ torr, $\dot{m} = 1.0$ g/s, $\nu = 5$ kHz, discharge power 30 W.

This demonstrates applicability and accuracy of this temperature measurement method at the present conditions. Note that the temperature has been measured in the plasma (as shown in Fig. 14), not in the flame region downstream, since $N_2(C^3\Pi_u \rightarrow B^3\Pi_g)$ emission there becomes very weak. For flame detection, both visual observations and visible emission spectra have been used. In particular, CH 4300 Å band system emission has been used as a flame indicator.

Figure 17 shows typical FT absorption spectra of the methane–air flow sampled downstream of the discharge section, at the equivalence ratio of $\varphi = 0.9$, $P = 100$ torr, $\dot{m} = 0.8$ g/s, $\nu = 40$ kHz, with and without the plasma. From Fig. 17, it can be seen that the use of the repetitively pulsed plasma results in a significant reduction of the methane concentration and an increase in concentrations of CO, CO_2, and H_2O in the flow. It can also be seen that oxidation of methane does not result in its conversion to acetylene (absorption band between 3230 and 3350 cm^{-1}), which has been observed in fuel rich mixtures excited by an RF discharge [13].

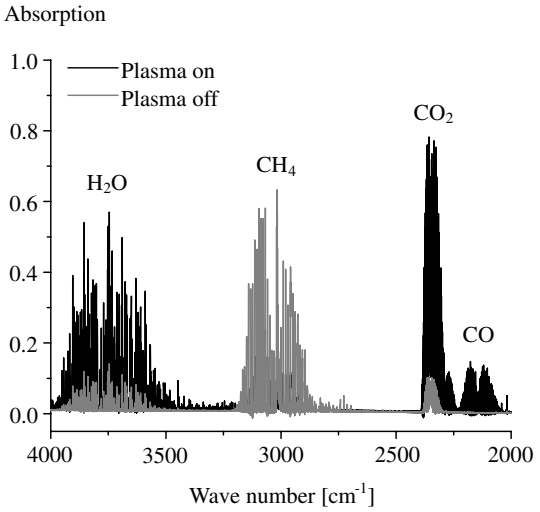

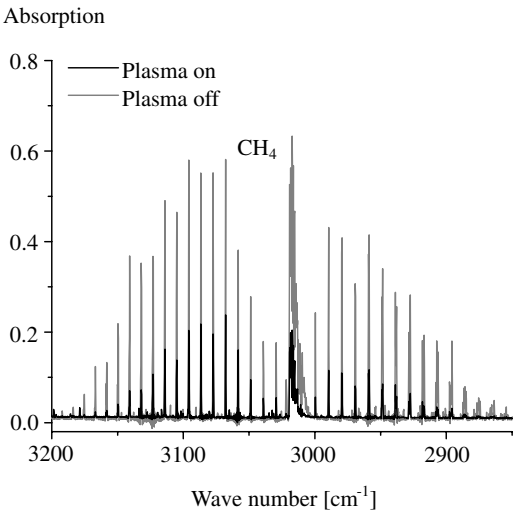

Fig. 17 FT absorption spectra of the flow sampled downstream of the discharge section, with and without repetitively pulsed plasma. Baseline case, methane–air mixture, $P = 100$ torr, mass flow rate 0.8 g/s, equivalence ratio 0.9, pulse repetition rate 40 kHz.

Figure 18 shows the results of temperature and reacted fuel fraction measurements in methane–air at $P = 100$ torr, $\dot{m} = 0.8$ g/s, and $\nu = 40$ kHz at different equivalence ratios. At these conditions, the time-averaged discharge power is 6 mJ · 40 kHz ≈ 240 W, which, in a quasi-one-dimensional flow, should result in air flow temperature rise of $\Delta T \approx 300$ K up to $T \approx 320$°C. From Fig. 18, it can be seen that the spectral temperature measured in air without the fuel (i.e., at $\varphi = 0$) is somewhat higher, $T = 390$°C. Because the plasma at these conditions appeared uniform and diffuse, without any hint of arc filaments, this suggests that the $N_2(C^3\Pi_u, \upsilon = 0)$ rotational temperature exceeds the actual flow temperature, and the use of an alternative spectroscopic method, such as CO infrared emission spectra, is desirable. One can also see that the $N_2(C^3\Pi_u, \upsilon = 0)$ temperature, used as an upper bound of the flow temperature, considerably increases as the fuel is added to the flow and peaks at the equivalence ratio of $\varphi = 0.6$–0.7, exceeding $T = 700$°C (see Fig. 18). Note that the reacted fuel fraction also peaks at these conditions, reaching 60–75%. Note, however, that in the entire range of the equivalence ratios, $\varphi = 0.3$–1.5, ignition has not been achieved and the flame has not been detected. This behavior of the plasma temperature and the reacted fuel fraction, in the absence of ignition, suggests two important conclusions: 1) significant amounts of methane can be oxidized by plasma chemical reactions in the repetitively pulsed plasma before ignition is achieved, and 2) the temperature rise is due to heat release in the net exothermic plasma chemical methane oxidation process.

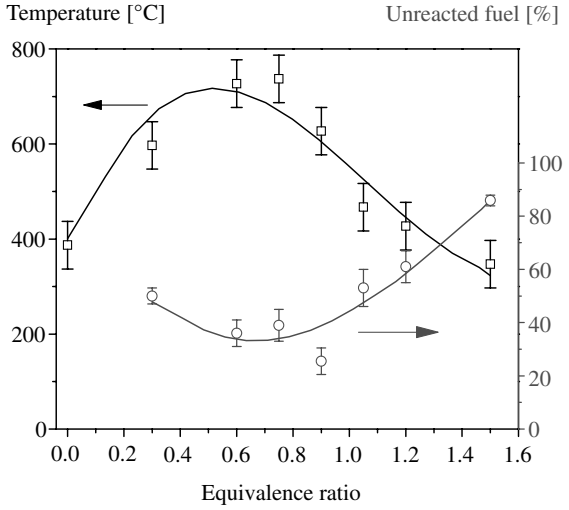

Fig. 18 Flow temperature in the discharge section and unreacted fuel fraction downstream of the plasma as functions of the equivalence ratio. Methane–air, $P = 100$ torr, mass flow rate 0.8 g/sec, pulse repetition rate 40 kHz. No flame was detected in the test section.

The dependence of the plasma temperature and of the reacted methane fraction on flow velocity $u = 11$–22 m/s, pulse repetition rate $\nu = 20$–50 kHz, and the test section pressure $P = 50$–150 torr were measured at the equivalence ratio of $\varphi = 0.9$, which produced the highest reacted fuel fraction at $\dot{m} = 0.8$ g/s (see Fig. 18). Significant methane oxidation was detected at the conditions where the air plasma temperature (before adding methane) was as low as $T = 200$°C (45% at $u = 11$ m/s and 35% at $\nu = 30$ kHz). However, ignition and a flame in methane–air mixtures were not observed in the entire range of the experimental conditions.

The results obtained in ethylene–air flows are similar to the methane–air results in several respects. The most significant difference between the ethylene and the methane experiments is that, in ethylene, ignition was produced and a flame extending through the test section (such as shown in Fig. 14) was detected at several experimental conditions. Figure 19 summarizes the results in ethylene–air mixtures at the baseline conditions, at $P = 70$ torr, $\dot{m} = 0.8$ g/s, $\nu = 40$ kHz, for different equivalence ratios. From Fig. 19, it can be seen that the temperature in the air plasma (without fuel) at these conditions is $T = 290$°C. When relatively small amounts of fuel are added to the air flow (at $\varphi = 0.4$ and 0.6), the flow

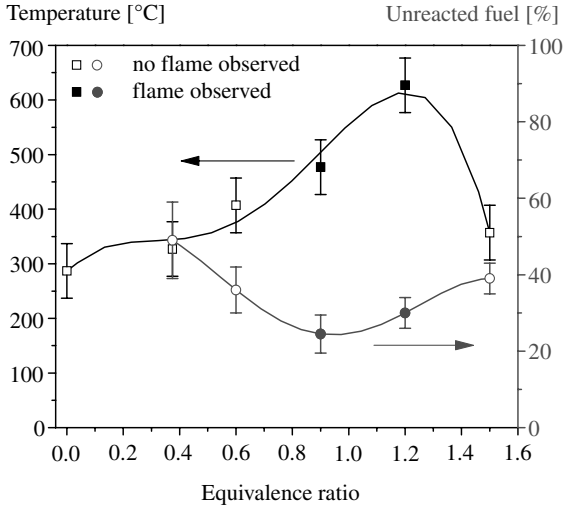

Fig. 19 Flow temperature in the discharge section and unreacted fuel fraction downstream of the plasma as functions of the equivalence ratio. Ethylene–air, $P = 70$ torr, mass flow rate 0.8 g/s, pulse repetition rate 40 kHz. Conditions at which ignition is achieved are marked with closed symbols.

temperature in the plasma noticeably increases, up to $T = 330$ and $T = 410$°C, respectively, and significant fractions of ethylene are oxidized ($51 \pm 10\%$ and $64 \pm 6\%$, respectively; see Fig. 19). Note that, at both these conditions, no flame was detected in the test section. Again, significant fuel oxidation in the plasma, with the resultant temperature rise, without producing ignition suggests that net exothermal fuel oxidation process is caused by plasma chemical reactions at relatively low temperatures. Note that, although hot spot (small arc filament) formation near the electrode surfaces and in the corners of the discharge sections remains a possibility, this has never been observed in the present experiments. Also, it seems extremely unlikely that such hot spots, if they indeed form in the plasma, may be responsible for oxidizing of up to two-thirds of the fuel without producing ignition.

Adding larger amounts of fuel to the flow (at $\varphi = 0.9$ and 1.2) resulted in flow ignition, with a flame produced downstream of the plasma and visible through the rectangular window (as shown in Fig. 14). The data measured at the conditions when the flow ignites are marked with closed symbols in Fig. 19 and subsequent figures. At these conditions, the burned fuel fraction was highest, $75 \pm 5\%$ and $70 \pm 4\%$, respectively, while the flow temperature in the plasma peaked $T = 630$°C at $\varphi = 1.2$ (see Fig. 19). Further increase of the equivalence ratio, up to $\varphi = 1.5$, did not produce ignition and resulted in a reduction of the oxidized fuel fraction, $61 \pm 4\%$, with a significant drop in the plasma temperature down to $T = 360$°C (see Fig. 19). This behavior suggests that, although the initial fuel oxidation in the plasma occurs due to plasma chemical reactions, ignition occurs only when the temperature rise due to heat generation in the plasma chemical oxidation process becomes sufficiently high.

To test whether the observed reduction of ethylene concentration is triggered by the electron impact dissociation of ethylene in the plasma or by plasma chemical processes involving oxygen, the air flow at the same baseline conditions was replaced by the nitrogen flow. At these conditions, the detected ethylene concentration reduction did not exceed a few percent, which is within the uncertainty of fuel concentration measurements in the present experiments, with weak acetylene bands detected in the absorption spectra. Very similar results have been obtained in methane–nitrogen flows. Because the pulse voltages in fuel–air and in fuel–nitrogen flows were similar, this result suggests that direct electron impact dissociation of ethylene and methane in the plasma is a relatively minor effect compared to reactions with species generated in the plasma in the presence of oxygen, such as O atoms and OH radicals. Also, our previous plasma-assisted combustion experiments using an RF discharge [13] show that oxidized fuel fractions (both ethylene and methane) in room air and in dry air flows were very close. This suggests that the effect of OH radicals on kinetics of plasma-assisted fuel oxidation is small, whereas O atoms may be the key species in the plasma fuel oxidation mechanism. As in our previous RF discharge ignition experiments [12], visible emission spectra of the plasma showed the presence of O and H atoms, as well as OH radicals generated by the discharge. When ignition was achieved, CH 4300 Å band system emission was also detected from the flame downstream of the plasma region (see Fig. 14).

Figure 20 shows the effect of the flow velocity through the test section on the temperature in the plasma and on the reacted fuel fraction. These measurements have been done at different mass flow rates, at the same pressure and pulse repetition rate, $P = 70$ torr and $\nu = 40$ kHz, respectively, and at the equivalence ratio of $\varphi = 1.2$, which produced the highest plasma temperature at $\dot{m} = 0.8$ g/s (flow velocity of $u = 15$ m/s). Figure 20 also shows the results of flow temperature measurements in air plasma (without fuel) at the same conditions. Again, the conditions when the flow ignites are marked with closed symbols. It can be seen that, although both the air flow and the fuel–air mixture temperature decrease with the flow velocity, the temperature of the air–fuel mixture is significantly higher. Comparing these results with the measurements of the reacted fuel fraction, also shown in Fig. 20, again suggests that this temperature increase is due to heat generation during fuel oxidation. Note that ignition was achieved at the flow velocities of $u = 15$, 20, and 25 m/s, that is, at the flow temperatures of $T = 290$, $T = 180$,

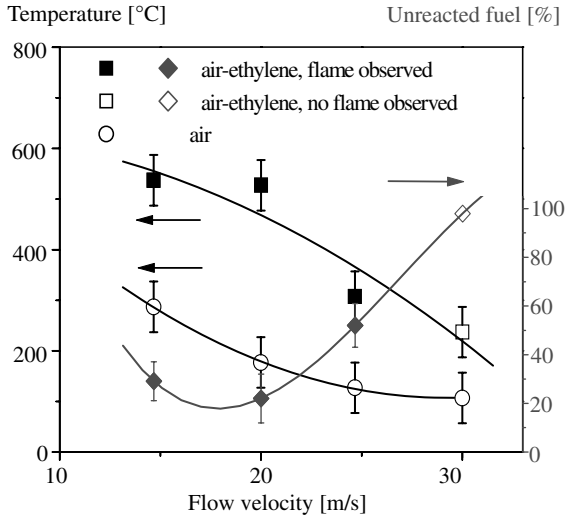

Fig. 20 Flow temperature in the discharge section and unreacted fuel fraction downstream of the plasma as functions of the flow velocity. Ethylene–air, $P = 70$ torr, equivalence ratio 1.2, pulse repetition rate 40 kHz. Closed symbols indicate conditions at which ignition is achieved and flame is detected in the test section.

and $T = 140$°C, respectively. At these conditions, the reacted fuel fraction is between 50 and 80% (see Fig. 20). Remembering that the $N_2(C^3\Pi_u, v = 0)$ temperature is an upper bound of the flow temperature, these results demonstrate that ethylene–air flows can be ignited by the repetitively pulsed plasma at very low plasma temperatures, with little flow preheating by the plasma.

Figure 21 summarizes the effect of the pulse repetition rate on the plasma temperature and the reacted fuel fraction. These measurements have been done at $\dot{m} = 0.8$ g/s ($u = 15$ m/s) and $P = 70$ torr, at the equivalence ratio of $\varphi = 1.2$. The results of flow temperature measurements in air plasma (without fuel) at the same conditions are also shown for comparison. The results demonstrate that both the flow temperature and the reacted fuel fraction increase with the pulse repetition rate. Ignition has been achieved at $\nu = 30, 40$, and 50 kHz, at the flow temperature as low as $T = 180$°C, when the reacted fuel fraction is $46 \pm 6\%$. At $\nu = 50$ kHz, the burned fuel fraction reaches $86 \pm 6\%$.

These results suggest that the repetitively pulsed discharge plasma may be developed into a low-temperature, large-volume ignition source. Kinetic mechanism of low-temperature plasma ignition remains not well understood. Note that kinetic modeling calculations

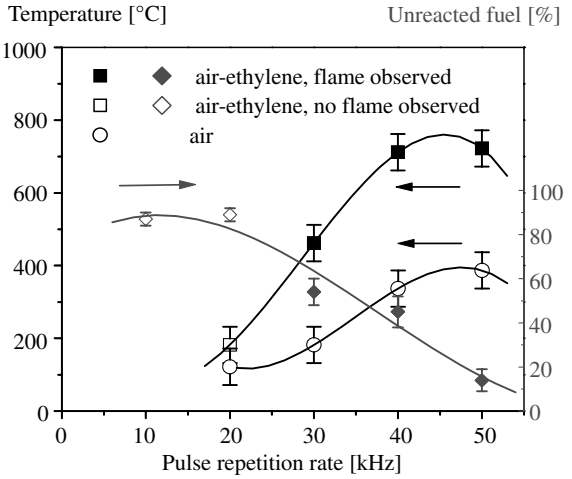

Fig. 21 Plasma temperature and unreacted fuel fraction vs pulse repetition rate. Ethylene–air, $P = 70$ torr, equivalence ratio 1.2, mass flow rate 0.8 g/s. Closed symbols indicate conditions at which ignition is achieved and flame is detected in the test section.

incorporating both the GRI-3.0 hydrocarbon combustion mechanism** and nonequilibrium pulsed discharge kinetics [59] do not reproduce the present experimental results. In particular, the calculations suggest that, at low temperatures, chain termination reactions are much faster than chain branching processes [10]. On the other hand, the experimental results indicate existence of a rapid low-temperature chain branching/radical multiplication process in the plasma. Experiments to measure O atom concentration in repetitively pulsed nanosecond discharge plasmas in air-fuel flows, and to detect such chain branching, are underway.

IV. Development of Electrically Excited Oxygen–Iodine Laser

The chemical oxygen–ion laser (COIL), which is one of a very few gas lasers scalable to high powers, is currently one of the most promising candidates for a high-power airborne laser system. Development of an electric discharge excited oxygen–iodine laser (DOIL) may potentially reduce the weight, complexity, and operational difficulties of the COIL laser. The key issue in DOIL development is achieving significant yields of singlet delta oxygen (SDO) molecules $O_2(a^1\Delta_g)$ in oxygen-containing low-temperature plasmas. The threshold SDO yield needed to achieve positive gain in oxygen–iodine mixtures strongly depends on temperature [25]:

$$\frac{[O_2(a^1\Delta)]}{[O_2(X^3\Sigma)]} = \frac{1}{1 + 1.5 \times \exp(403/T)} \tag{4}$$

14.8% at $T = 300$ K and only 1.2% at $T = 100$ K. Therefore, the flow temperature in the laser cavity needs to be low, which can be achieved by a rapid supersonic flow expansion, downstream of the electric discharge section. Recent RF discharge experiments in O_2–He mixtures, followed by a $M = 2$ expansion, demonstrated both positive gain on a 1315 nm iodine atom transition [22] and cw lasing with a 510 mW output power at the laser cavity temperature of 190 K [25,26]. However, the use of this approach at high Mach numbers also requires operating at rather high stagnation pressures. Also, to optimize the $O_2(a^1\Delta)$ yield in the plasma, the discharge should operate at E/N values where the energy input into the target $O_2(a^1\Delta)$ state is maximum, $E/N < 1 \cdot 10^{-16}$ V · cm^2 [19,20,28]. These E/N values are considerably lower than typically achieved in self-sustained nonequilibrium electric discharges, $E/N \sim (1\text{–}10) \cdot 10^{-16}$ V · cm^2. Therefore, optimizing energy input into singlet delta oxygen at high pressures suggests the use of the crossed pulser-sustainer discharge discussed in Sec. II, which offers both stable operation at high pressures and independent control of sustainer E/N.

A. Experimental

The experiments have been conducted at a blowdown facility designed for development and testing of an electrically pumped oxygen–iodine laser [28–30]. Premixed helium/oxygen flow is delivered to the test section via a 1-in.-diam, 15-ft-long supply line. The discharge section, the overall view of which is shown in Fig. 22, is made of acrylic plastic and has a rectangular inner cross section of 5×2 cm. Two rectangular dc electrodes, each 5 cm long and 2 cm wide, and two square-shaped pulsed electrodes, 5×5 cm, are flush mounted in the side walls and in the top/bottom walls of the discharge section, respectively (see Fig. 22). The dc electrodes are made of copper and are exposed to the flow. Each pulsed electrode plate, also made of copper, is insulated from the flow by a dielectric macor ceramic plate approximately 1 mm thick. On the opposite side, the pulsed electrodes are covered by acrylic plastic plates. Both sets of electrodes are located at the same streamwise location to form a crossed pulser/dc sustainer discharge, as shown in Fig. 22. The overall length of the test section is about 12 cm, with a crossed discharge length of 5 cm. Two optical access windows are located downstream of the discharge section, as shown in Fig. 22.

**http://www.me.berkeley.edu/gri_mech/

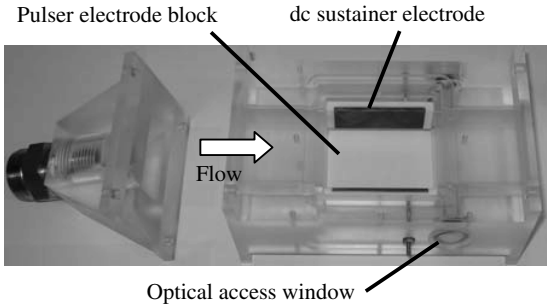

Fig. 22 Photograph of the discharge test section with the top pulsed electrode removed. Flow is left to right.

The electrodes are connected to a Chemical Physics Technologies pulsed plasma generator, described in Sec. II.A. The pulse voltage and current are measured using a Tektronix P6015A high-voltage probe, a low-capacitance resistive current probe, and a LeCroy Wavepro 7100A digital oscilloscope. The dc sustainer electrodes are powered by a Universal Voltronics high-current, low-voltage (4 A, 5 kV, 20 kW) dc power supply, operated in the voltage-stabilized mode. Adjustable high-power ballast resistors (Powerohm, 1050 W) are connected in series with the dc power supply to limit the maximum sustainer current. In the present experiments, the ballast resistance has been set at $R = 1.0$ kΩ.

The discharge section is followed by a contoured $M = 3$ nozzle and a supersonic section (see Fig. 23). The nozzle throat dimensions are 5×0.32 cm, and the nozzle exit dimensions are 5×1 cm. The discharge section/nozzle throat area ratio $A/A^* = 6.25$ corresponds to the discharge section Mach number of $M \approx 0.1$ for $\gamma = 1.625$, so that the discharge section serves as the nozzle plenum. The discharge section pressure (close to stagnation pressure) and the mixture composition can be varied independently. In the present experiments, the stagnation pressure was set at $P_0 = 60$–120 torr (laser cavity pressure of 2–4 torr). At these conditions, the mass flow rate of a 10% O_2/90% He mixture was 1.1 or 2.2 g/s. The top and bottom walls of the supersonic section (the laser cavity) are diverging at 1.5 deg each to provide the boundary-layer relief. The bottom wall of the cavity is equipped with 15 static pressure ports at five streamwise and three transverse locations to monitor the supersonic flow quality during operation. Plastic inserts, transparent for both visible and 1.3 μm infrared radiation, are flush mounted in the side walls of the supersonic section and span its entire length and height from the nozzle exit, providing optical access to the entire supersonic flow (see Fig. 23). The flow exhausts to a 1000 ft^3 vacuum tank. Between the runs, the tank is pumped down to $\sim$0.1 torr using a Stokes 212-H 150 cfm vacuum pump. The vacuum tank/pumping capacity provides steady-state run times in the $M = 3$ laser cavity of up to approximately 20 s.

Two stainless steel arms, 1 in. in diameter and 6 in. long each, are attached to the cavity side walls at the downstream end of the cavity for small signal gain measurements and laser power measurements (see Fig. 23). For the gain measurements, stainless steel flanges

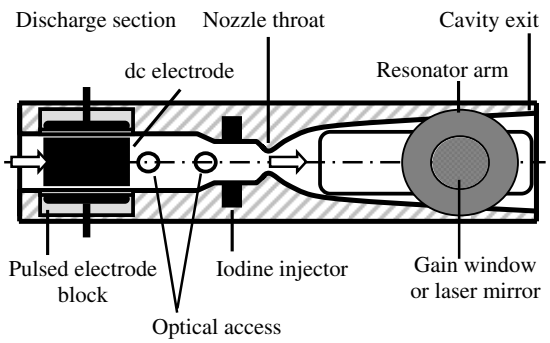

Fig. 23 Schematic of the discharge section/nozzle/laser cavity assembly.

10 mm in diameter, wedged, and antireflection-coated BK-7 glass windows are attached to the end of the arms. For the laser power measurements, the gain window flanges are replaced with two adjustable vacuum mirror mounts, attached to the end of the arms to form a stable resonator. In the present measurements, we used two Los Gatos Research mirrors with the 99.99% reflectivity at 1315 nm and the radius of curvature of 1 m. Both the gain windows and the laser mirrors are separated by approximately 40 cm. This modular arrangement allowed gain and laser power measurements at the same location and at the same flow conditions. To protect gain windows and laser mirrors from iodine deposits, two auxiliary helium curtain flows are injected into the supersonic cavity on both sides of the main $M = 3$ flow using two $M = 3.5$ nozzles. In addition, the resonator arms can be independently purged by separate helium flows.

Iodine vapor is added to the main flow using an iodine metering/delivery system developed at Physical Sciences, Inc., (PSI). Iodine vapor is produced by passing helium carrier gas over heated iodine crystals. I_2 concentration in the flow is measured by molecular iodine continuum absorption at 488 nm [60]. The iodine–helium mixture is injected into the flow through two stainless steel injection blocks upstream of the nozzle throat (see Fig. 23). In the present experiments, iodine crystals were heated up to 60°C, producing I_2 vapor flow rate of up to 140 μmol/s, at the He carrier flow rate of up to 60 mmol/s. All flows through the test section (main oxygen/helium mixture, curtain helium, iodine vapor/helium mixture, and purge helium) are started simultaneously using remotely controlled solenoid valves.

Small signal gain at 1315 nm in the $M = 3$ cavity is measured by tunable diode laser absorption spectroscopy using the PSI iodine scan sensor [61,62]. In the absence of excited iodine atoms, the sensor measures absorption by the ground state I atoms. When excited iodine atoms I^* are generated by energy transfer from SDO, the sensor measures a combination of absorption and stimulated emission. Positive gain across the optical path of $L = 5$ cm is measured when population inversion is achieved in the flow ($[I^*]/[I] > 1/2$). The recorded spectra, each averaged over a 0.5 s period, are used to calculate optical gain/loss at the line center and the flow temperature from the line shape profile. The laser output power is detected using a New Focus Model 5842 infrared card and measured by a Scientech power meter.

Visible and infrared emission spectroscopy measurements have been conducted using a 0.5 m monochromator, 600 g/mm grating blazed at 1 μm, and a Roper Scientific liquid nitrogen-cooled 1-D array 1024 pixel InGaAs PDA OMA V camera. The emission signal was collected using a Thor Labs 1-m-long fiber optic bundle with a 1-in.-diam collimator on the collection end. The collimator was positioned in front of an optical access window, and the opposite end of the fiber optic bundle was placed in front of the spectrometer slit. The use of the fiber optic link greatly improved alignment of the optical diagnostics system. The $O_2(a^1\Delta)$ concentration in the discharge afterglow and the SDO yield were evaluated by calibration of the fiber optics/OMA/CCD camera signal collection system using an Infrared Systems calibrated blackbody source IR-564.

B. Results and Discussion

Static pressure measurements at multiple locations in the supersonic cavity showed that a uniform $M = 2.9$–3.1 flow is produced, with good pressure matching between the main flow and the curtain flows achieved within about 1 s after the flows started. After the pressure is stabilized, the crossed discharge is initiated by starting the high-voltage, high repetition rate pulse sequence. Both the dc power supply and the optical diagnostics system are triggered by the pulsed power supply and remain on only for the duration of the high-voltage pulse train. Typical pulse peak voltage is 15 kV and pulse FWHM is 25 ns. At these conditions, the peak pulse current is approximately 65 A and the pulse energy coupled to the flow is 2.1 mJ. The pulse energies, measured from the pulse voltage and current oscillograms, are in the 2–3 mJ range, which, at the pulse repetition rate of $\nu = 40$ kHz, corresponds to the time-averaged power of 80–120 W.

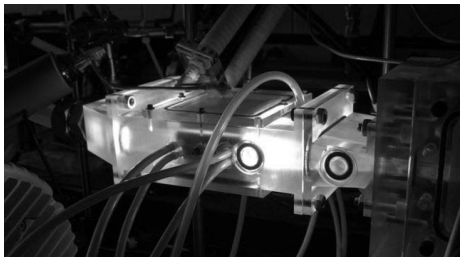

Fig. 24 Photograph of the discharge section in operation. 10% O_2 in helium, $P = 120$ torr, pulse repetition rate 50 kHz. Flow is left to right.

Figure 24 shows a photograph of the crossed discharge in a 10% O_2–He flow at $P_0 = 120$ torr and $\nu = 50$ kHz. Typical run time with the crossed discharge turned on was from 5 to 15 s. Figure 25 show oscillograms of the sustainer current and voltage, as well as the sustainer discharge power coupled to the flow and the estimated reduced electric field E/N in the crossed discharge in a 10% O_2–He flow at $P_0 = 60$ torr and $\nu = 40$ kHz. In Fig. 25, the dc power supply voltage was $U_{PS} = 1.5$ kV, with the ballast resistor of $R = 1.0$ kΩ. In Fig. 25, E/N is evaluated based on the flow number density at room temperature, neglecting the cathode voltage fall in the sustainer discharge. From Fig. 25, it can be seen that, at the dc voltage of $U_{PS} = 1.5$ kV, the sustainer current between the pulses decreases from approximately $I = 1.1$ to about $I = 0.75$ A, whereas the sustainer voltage $U = U_{PS} - IR$ increases from $U = 0.4$ to $U = 0.75$ kV. The sustainer discharge power and E/N at these conditions vary from 0.45 to 0.55 kW and from 0.45×10^{-16} to 0.75×10^{-16} V · cm^2, respectively. These E/N values remain far too low for the dc discharge to become self-sustained. The discharge terminated as soon as the pulser was turned off.

Figure 26 shows time-averaged values of the reduced electric field in the sustainer discharge in a 10% O_2—90% He mixture at $P_0 = 60$ and 120 torr, plotted against the time-averaged discharge power. The discharge power was varied by changing the dc power supply voltage. It can be seen that the sustainer power coupled to the flow at $P_0 = 60$ and 120 torr ranges from 0.5 to 1.6 kW, and from 0.9 to 2.2 kW, respectively. From Fig. 26, one can also see that the reduced

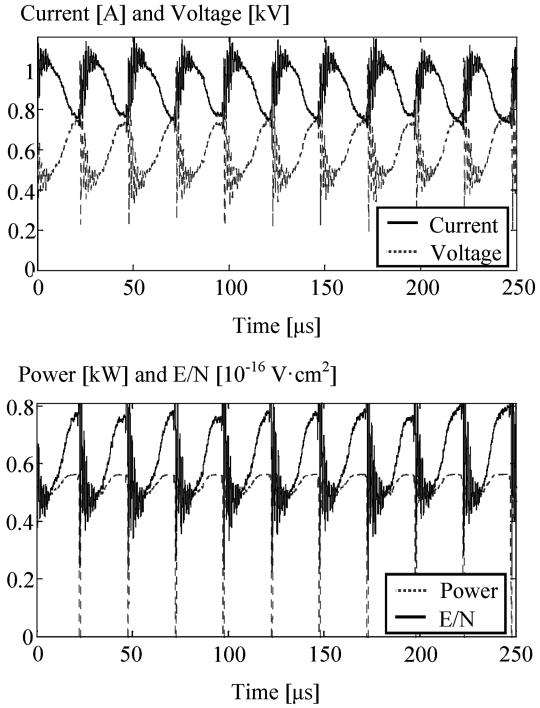

Fig. 25 Oscillograms of dc sustainer current, voltage, power, and reduced electric field E/N in the crossed discharge. 10% O_2 in helium, $P = 60$ torr, $U = 1.5$ kV, pulse repetition rate 40 kHz.

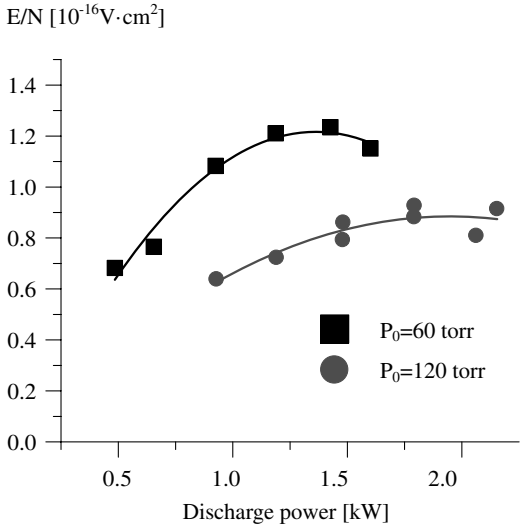

Fig. 26 Time-averaged reduced electric field vs time-averaged sustainer discharge power. 10% O_2 in helium.

electric field in the sustainer discharge increases with the discharge power. Comparing the results of Fig. 26 with the modeling calculations predicting the energy balance in a nonequilibrium plasma as a function of E/N, using a Boltzmann equation solver [28], one could expect approximately 15–20% of the input discharge power in the 10% O_2–He mixture to go to electron impact excitation of the $O_2(a^1\Delta)$ state.

Figure 27 shows typical $O_2(a^1\Delta \rightarrow X^3\Sigma)$ infrared emission spectrum, (0,0) band with the band center at 1.268 μm, in a 10% O_2–He mixture at $P_0 = 60$ torr. The SDO yield was inferred from the experimental infrared emission spectra using blackbody calibration. During the calibration, both the signal collection volume sampled by the fiber optics collimator and contributions of different parts of the collection volume into the overall collected signal were determined. The calibration is significantly simplified by the fact that the flow is optically thin for the $O_2(a^1\Delta \rightarrow X^3\Sigma)$ emission, due to an extremely long radiative lifetime of the $O_2(a^1\Delta)$ state, with the Einstein coefficient for spontaneous emission of $A_{rad} = 2.2 \times 10^{-4}$ s^{-1} (radiative lifetime of 76 min) [63,64]. Partially rotationally resolved $O_2(b^1\Sigma \rightarrow X^3\Sigma)$ emission spectra have been used to infer the flow temperature both in the discharge section and in the supersonic laser cavity. Figure 28 shows a (0,0) band of the $O_2(b^1\Sigma \rightarrow X^3\Sigma)$ spectrum in a 10% O_2–He $M = 3$ flow at $P_0 = 60$ torr, $U_{PS} = 2.5$ kV. Figure 28 also shows the synthetic

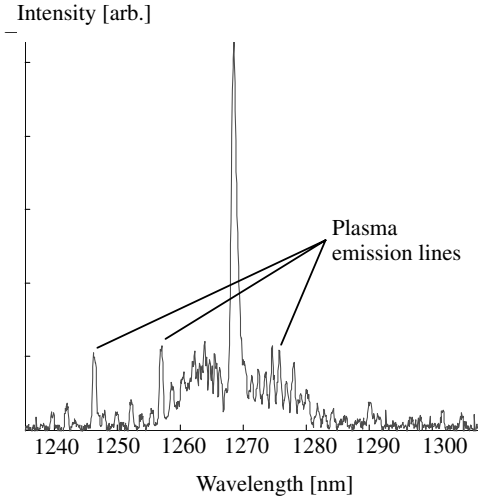

Fig. 27 Typical $O_2(a^1\Delta \rightarrow X^3\Sigma)$ emission spectrum. 10% O_2 in helium, $P_0 = 60$ torr, $U_{PS} = 2.5$ kV.

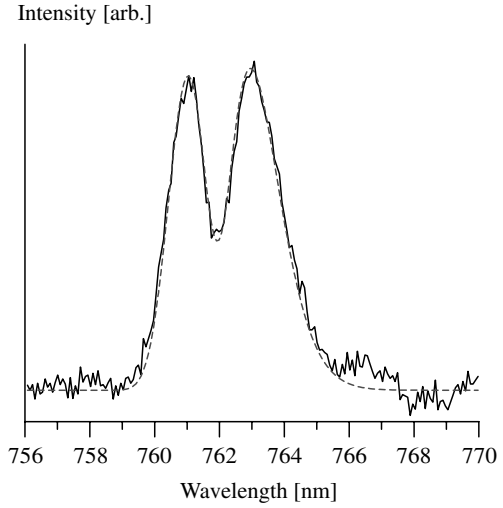

Fig. 28 Comparison of the experimental and synthetic $O_2(b^1\Sigma \rightarrow X^3\Sigma)$ emission spectra in a $M = 3$ laser cavity. 10% O_2 in helium, $P_0 = 60$ torr, $P = 1.9$ torr, $U_{PS} = 2.5$ kV, $T = 120$ K.

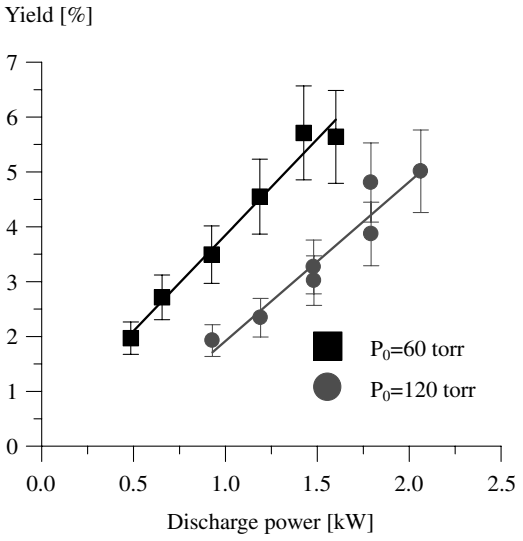

Fig. 29 $O_2(a^1\Delta)$ yield vs sustainer discharge power in 10% O_2–He flows.

spectrum calculated at the rotational temperature of $T = 120 \pm 10$ K. The spectroscopic constants and the rotational line strengths for the synthetic spectrum are taken from [65,66].

Figure 29 shows the SDO yields vs the sustainer discharge power, measured in 10% O_2–He flows at two different discharge pressures, $P_0 = 60$ and 120 torr. The error bars in Fig. 29 indicate a combined uncertainty in the Einstein coefficient, flow temperature, and contribution of the atomic emission lines in the $O_2(a^1\Delta \rightarrow X^3\Sigma)$ spectra (see Fig. 27). From Fig. 29, it can be seen that the yield increases roughly proportional to the discharge power, up to approximately 5.7% at $P_0 = 60$ torr, 1.6 kW, and up to 5.0% at $P_0 = 120$ torr, 2.1 kW.

Flow temperature and pressure measurements in 10% O_2—90% He flows, at the conditions when the highest SDO yields were achieved, are summarized in Table 1. The static temperature in a $M = 3$ flow at the end of the supersonic test section is calculated from the stagnation temperature T_0 measured in the discharge section, using a quasi-one-dimensional isentropic flow theory. From Fig. 28, it can be seen that the calculated temperature is consistent with the measured temperature. The results of Table 1 show that, at the flow temperatures achieved at the end of the $M = 3$ cavity, $T = 100$–110 K, the measured SDO yields exceed gain threshold yields for these temperatures by more than a factor of 3. Therefore, the present results suggest that yields measured in the present experiments may be sufficient for achieving positive gain in the supersonic cavity. Finally, SDO yield measurements in three different oxygen–helium mixtures, with 10, 15, and 20% oxygen fraction, at the same dc voltage $U_{PS} = 2.5$ kV, showed that increasing the oxygen mole fraction in the mixture only weakly affects the yield. This suggests that the crossed pulser-sustainer discharge singlet oxygen generator can be successfully used for an electrically excited oxygen–iodine laser in a wide range of oxygen concentrations in the flow.

This conclusion was verified by gain and laser power measurements in the $M = 3$ laser cavity [29,30]. Figure 30 shows a typical gain line shape measured during a single run in a 15% O_2–He flow, at $P_0 = 80$ torr, $\nu = 34$ kHz, $U_{PS} = 2.5$ kV, $I = 1.35$ A, and I_2 flow rate of 50 μmol/s. With both the pulsed discharge and the dc discharge operating, excited iodine atoms are produced in the flow by energy transfer from $O_2(a^1\Delta)$ to ground state iodine atoms. This produces population inversion and results in an optical gain of up to 0.036%/cm, as shown in Fig. 30. Figure 30 also shows a typical Doppler fit to the experimental line shape, yielding translational temperature in the cavity of $T = 105 \pm 10$ K. The temperature, inferred from both absorption and gain line shapes, remains nearly constant (within the uncertainty of ± 10 K) during the entire run. This is in good agreement with the rotational temperature measured by emission spectroscopy, $T = 120 \pm 15$ K (see Fig. 28).

At these conditions, a single-pass gain, about 0.2%, exceeds the laser mirror loss, about 0.01%, by more than order of magnitude. Also, the measured gain is about a factor of 6 higher than measured in [25] at the conditions when lasing was detected. This suggested that lasing could also be achieved at the present experimental conditions. Indeed, replacing the gain windows with the laser mirrors demonstrated cw lasing, detected using both the infrared card and the power meter. Figure 31 shows an elliptic shape spot, approximately 1 cm long, detected on an infrared card placed across the laser beam. Figure 32 shows the laser output power measured by the power meter. Because the response time of the power meter ranges from 5 to 10 s, the signal increases with time and does not quite stabilize at the end of a 7 s run, showing the output power at the end of the run of approximately 0.28 W. This number is equal to the combined power of two laser beams coming through two identical 99.99% output coupler mirrors, with approximately equal powers of 0.14 W each. As can be seen from Fig. 32, this result represents the lower bound of the laser output power.

We expect that the use of a supersonic diffuser placed downstream of the laser cavity would considerably increase the steady-state run time at the design resonator Mach number $M = 3.0$ and allow laser power measurements at the steady-state flow conditions. Ongoing and future work to increase the output power includes operating at higher plenum pressures, reducing the O atom concentration in the discharge by NO titration [23,26], and iodine vapor dissociation in an auxiliary electric discharge.

Table 1 Summary of SDO measurements in a 10% O_2–He $M = 3$ flow

P_0, torr	$\dot{m}$, g/s	T_0, K	Discharge power, kW	P_{cavity}, torr	M_{cavity}	T_{cavity}, K	SDO yield, %	Threshold yield, %
60	1.5	420 ± 25	1.6	1.8	3.0	110	5.7 ± 0.75	1.7
120	3.0	400 ± 25	2.1	3.2	3.0	105	5.0 ± 0.5	1.4

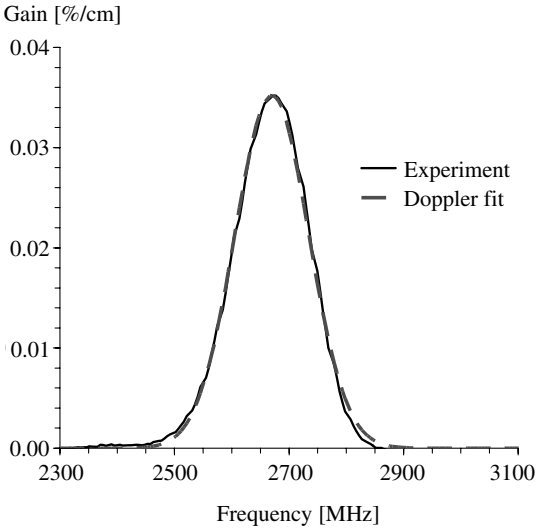

Fig. 30 Absorption/gain line shapes. 15% O_2–He flow, $P_0 = 80$ torr, $\nu = 34$ kHz, $U_{PS} = 2.5$ kV, $I = 1.35$ A, I_2 flow rate 50 μmol/s. Doppler fits indicate the flow temperature of $T = 105 \pm 10$ K.

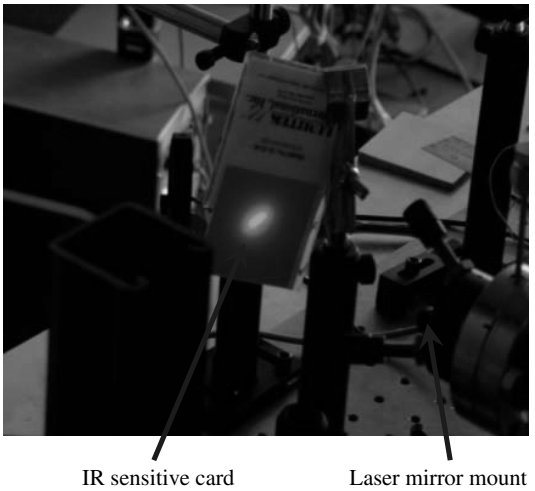

Fig. 31 Photograph of the laser beam spot on an infrared sensitive card. 15% O_2–He flow, $P_0 = 60$ torr, $\nu = 34$ kHz, $U_{PS} = 2.5$ kV, $I = 1.2$ A, I_2 flow rate 50 μmol/s.

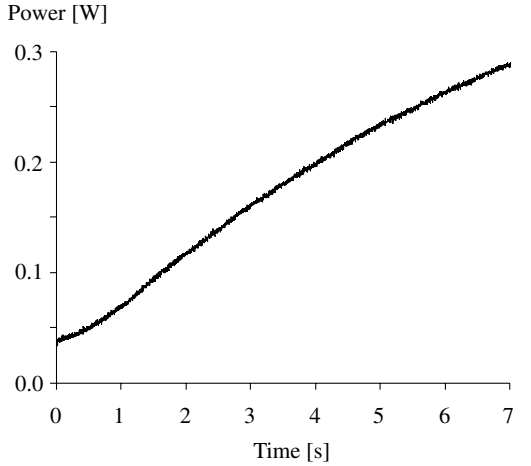

Fig. 32 Laser power (two laser beams combined) measured by the power meter at the conditions of Fig. 31. The signal increases with time due to a long response time of the power meter (5–10 s).

V. Conclusions

The results discussed in Secs. II, III, and IV demonstrate significant potential of the use of high-voltage, nanosecond pulse duration, high pulse repetition rate discharges for aerospace applications. These results demonstrate key advantages of these discharges, which combine 1) stability at high pressures, high flow Mach numbers, and high-energy loadings by the sustainer discharge, 2) high-energy fractions going to ionization and molecular dissociation, and 3) targeted energy addition capability provided by independent control of the reduced electric field of the dc sustainer discharge. These unique capabilities make possible the generation of stable, volume-filling, low-temperature plasmas and their use for high-speed flow control, nonthermal flow ignition, and efficient generation of excited metastable species for molecular lasers.

In particular, the crossed pulser-sustainer discharge was used to produce ionization in $M = 3$ nitrogen and air flows in the presence of a transverse dc electric field and transverse magnetic field. The MHD effect on the low-temperature flows was detected from the laser differential interferometry and static pressure measurements. Retarding Lorentz force applied to cold $M = 3$ nitrogen and air flows produces an increase of the density fluctuation intensity by up to 2 dB (about 25%), compared with the accelerating force of the same magnitude. Also, retarding Lorentz force applied to the flow produces a static pressure increase of up to 17–20%, whereas accelerating force of the same magnitude results in a static pressure increase of up to 5–7%. Both of these effects are produced for two possible combinations of the magnetic field and transverse current directions producing the same Lorentz force direction (both for accelerating and retarding force). This demonstrates that the observed effects are indeed due to the MHD interaction, and not due to Joule heating of the flow in the crossed discharge. The measured static pressure changes are consistent with the quasi-one-dimensional MHD flow theory, which shows that the retarding Lorentz force increases the static pressure rise produced by Joule heating of the flow in the discharge, while the accelerating Lorentz force reduces the pressure rise. This result provides first direct evidence of cold supersonic flow deceleration by Lorentz force.

The pulsed discharge (without sustainer) was also used to produce plasma chemical fuel oxidation, ignition, and flameholding in premixed methane–air and ethylene–air flows, in a wide range of equivalence ratios, flow velocities, and pressures. The flame originates in the plasma, extends downstream through the test section, and remains stable as long as the plasma is on. Plasma-assisted ignition occurs at a low discharge powers and low plasma temperatures, 150–300°C. At these conditions, the reacted fuel fraction, measured by the FTIR absorption spectroscopy, is up to 80%. The experiments also demonstrate significant methane and ethylene oxidation, with the resultant temperature rise, at the conditions when there is no ignition and no flame detected in the test section. At these conditions, fuel oxidation occurs entirely due to plasma chemical reactions. The results suggests the following conclusions: 1) significant amounts of hydrocarbons can be oxidized by low-temperature plasma chemical reactions before ignition is achieved, 2) the detected plasma temperature rise is due to heat release in the net exothermic plasma chemical fuel oxidation process, and 3) ignition occurs when the temperature rise due to heat generation in the plasma chemical oxidation process becomes sufficiently high. In other words, low-temperature plasma chemical fuel conversion and the resultant flow heating "open the door" to ignition.

Finally, the pulser-sustainer discharge was used to generate singlet oxygen at high pressures. In this application, the sustainer discharge voltage could be independently varied to choose the reduced electric field value such as to maximize the sustainer energy input into electron impact excitation of singlet delta oxygen. The results demonstrate operation of a stable and diffuse crossed discharge in oxygen–helium mixtures at pressures of 60–120 torr and sustainer discharge powers of up to 1.6–2.2 kW. The reduced electric field in the positive column of the sustainer discharge in O_2–He flows was varied from 0.6×10^{-16} to 1.2×10^{-16} V · cm^2. Singlet delta

oxygen yield at these conditions, up to 5.7% at a flow temperature of 420 K, was inferred from the integrated intensity of the (0,0) band of the $O_2(a^1\Delta \rightarrow X^3\Sigma)$ infrared emission spectra calibrated using a blackbody source. The results show that the $O_2(a^1\Delta)$ yield increases nearly proportionally to the sustainer discharge power and remains nearly independent of the O_2 fraction in the mixture (up to 20%). The results also show that the measured singlet delta oxygen yield exceeds the threshold yield at the flow temperatures achieved in the $M = 3$ laser cavity, $T = 100$–110 K, by about a factor of 3. Small signal gain on the 1315 nm iodine atom transition and the laser output power are measured in the $M = 3$ supersonic cavity downstream of the discharge section. In a 15% O_2–85% He mixture, at a discharge pressure of 80 torr and discharge power of 1.55 kW, the highest gain measured in the $M = 3$ cavity is 0.04%/cm, at the flow temperature of $T = 105$ K. The laser output power measured at a pressure of 60 torr and discharge power of 1.55 kW is 0.28 W.

Acknowledgments

This work has been supported by U.S. Air Force Office of Scientific Research grants FA9550-05-1-0085 and FA9550-05-1-0312, Phase I Air Force Office of Scientific Research Small Business Innovation Research grant, Phase II Air Force Office of Scientific Research Small Business Technology Transfer Program grant F49620-02-C-0054, and by Phase II Missile Defence Agency Strategic Technology Transfer Report grant, technically directed by Directed Energy Directorate of Air Force Research Laboratory. We would like to express our sincere gratitude to Sergey Gorbatov and Fedor Plevako from Chemical Physics Technologies for continuing support and collaboration, as well as for their help in setting up and operating the pulsed power supplies.

References

[1] Meyer, R., Nishihara, M., Hicks, A., Chintala, N., Cundy, M., Lempert, W. R., Adamovich, I. V., and Gogineni, S., "Measurements of Flow Conductivity and Density Fluctuations in Supersonic Nonequilibrium MHD Flows," *AIAA Journal*, Vol. 43, No. 9, 2005, pp. 1923–1930. doi:10.2514/1.13736

[2] Nishihara, M., Jiang, N., Rich, J. W., Lempert, W. R., Adamovich, I. V., and Gogineni, S., "Low-Temperature Supersonic Boundary Layer Control Using Repetitively Pulsed MHD Forcing," *Physics of Fluids*, Vol. 17, No. 10, 2005, p. 106102. doi:10.1063/1.2084227

[3] Nishihara, M., Rich, J. W., Lempert, W. R., Adamovich, I. V., and Gogineni, S., "Low-Temperature $M = 3$ Flow Deceleration by Lorentz Force," *Physics of Fluids*, Vol. 18, No. 8, 2006, p. 086101. doi:10.1063/1.2265011

[4] Murray, R. C., Zaidi, S. H., Carraro, M. R., Vasilyak, L. M., Macheret, S. O., Shneider, M. N., and Miles, R. B., "Magnetohydrodynamic Power Generation Using Externally Ionized, Cold, Supersonic Air as Working Fluid," *AIAA Journal*, Vol. 44, No. 1, 2006, pp. 119–127. doi:10.2514/1.11611

[5] Zaidi, S., Smith, T., Macheret, S., and Miles, R., "Snowplow Surface Discharge in Magnetic Field for High Speed Boundary Layer Control," *44th AIAA Aerospace Sciences Meeting and Exhibit*, AIAA Paper 2006-1006, 2006.

[6] Shang, J. S., Kimmel, R., Hayes, J., Tyler, C., and Menart, J., "Hypersonic Experimental Facility for Magnetoaerodynamic Interactions," *Journal of Spacecraft and Rockets*, Vol. 42, No. 5, 2005, pp. 780–789. doi:10.2514/1.8579

[7] Bozhenkov, S. A., Starikovskaya, S. M., and Starikovskii, A. Yu., "Nanosecond Gas Discharge Ignition of H_2- and CH_4-Containing Mixtures," *Combustion and Flame*, Vol. 133, Nos. 1–2, 2003, pp. 133–146. doi:10.1016/S0010-2180(02)00564-3

[8] Starikovskaia, S. M., Kukaev, E. N., Kuksin, A. Yu., Nudnova, M. M., and Starikovskii, A. Yu., "Analysis of the Spatial Uniformity of the Combustion of a Gaseous Mixture Initiated by a Nanosecond Discharge," *Combustion and Flame*, Vol. 139, No. 3, 2004, pp. 177–187. doi:10.1016/j.combustflame.2004.07.005

[9] Mintoussov, E., S. Pancheshnyi, and Starikovskii, A., "Propane-Air Flame Control by Non-Equilibrium Low-Temperature Pulsed Nanosecond Barrier Discharge," *42nd AIAA Aerospace Sciences Meeting and Exhibit*, AIAA Paper 2004-1013, 2004.

[10] Starikovskii, A. Yu., "Plasma Supported Combustion," *Proceedings of the Combustion Institute*, Vol. 30, No. 2, 2005, pp. 2405–2417. doi:10.1016/j.proci.2004.08.272

[11] Anikin, N. B., Starikovskaya, S. M., and Starikovskii, A. Yu., "Oxidation of Saturated Hydrocarbons Under the Effect of Nanosecond Pulsed Space Discharge," *Journal of Physics D: Applied Physics*, Vol. 39, No. 15, Aug. 2006, pp. 3244–3252. doi:10.1088/0022-3727/39/15/006

[12] Chintala, N., Meyer, R., Hicks, A., Bao, A., Rich, J. W., Lempert, W. R., and Adamovich, I. V., "Non-Thermal Ignition of Premixed Hydrocarbon-Air Flows by Nonequilibrium RF Plasma," *Journal of Propulsion and Power*, Vol. 21, No. 4, 2005, pp. 583–590. doi:10.2514/1.10865

[13] Chintala, N., Bao, A., Lou, G., and Adamovich, I. V., "Measurements of Combustion Efficiency in Nonequilibrium RF Plasma Ignited Flows," *Combustion and Flame*, Vol. 144, No. 4, 2006, pp. 744–756. doi:10.1016/j.combustflame.2005.08.040

[14] Lou, G., Bao, A., Nishihara, M., Keshav, S., Utkin, Y. G., Rich, J. W., Lempert, W. R., and Adamovich, I. V., "Ignition of Premixed Hydrocarbon-Air Flows by Repetitively Pulsed, Nanosecond Pulse Duration Plasma," *Proceedings of the Combustion Institute*, Vol. 31, No. 2, Jan. 2007, pp. 3327–3334. doi:10.1016/j.proci.2006.07.126

[15] Kim, W., Do, H., Mungal, M. G., and Cappelli, M. A., "Investigation of NO Production and Flame Structure in Plasma Enhanced Premixed Combustion," *Proceedings of the Combustion Institute*, Vol. 31, No. 2, Jan. 2007, pp. 3319–3326. doi:10.1016/j.proci.2006.07.107

[16] Galley, D., Pilla, G., Lacoste, D., Ducruix, S., and Laux, C., "Plasma-Enhanced Combustion of a Lean Premixed Air-Propane Turbulent Flame Using a Nanosecond Repetitively Pulsed Plasma," *43rd AIAA Aerospace Sciences Meeting and Exhibit*, AIAA Paper 2005-1193, 2005.

[17] Napartovich, A. P., Deryugin, A., and Kochetov, I., "Discharge Production of the Singlet Delta Oxygen for an Iodine Laser," *Journal of Physics D: Applied Physics*, Vol. 34, No. 12, June 2001, pp. 1827–1833. doi:10.1088/0022-3727/34/12/310

[18] Schmiedberger, J., and Fujii, H., "Radio-Frequency Plasma Jet Generator of Singlet Delta Oxygen with High Yield," *Applied Physics Letters*, Vol. 78, No. 18, 2001, pp. 2649–2651. doi:10.1063/1.1367899

[19] Ionin, A. A., Klimachev, Y. M., Kotkov, A. A., Kochetov, I. V., Napartovich, A. P., Seleznev, L. V., Sinitsyn, D. V., and Hager, G. D., "Non-Self-Sustained Electric Discharge in Oxygen Gas Mixtures: Singlet Delta Oxygen Production," *Journal of Physics D: Applied Physics*, Vol. 36, No. 8, 2003, pp. 982–989. doi:10.1088/0022-3727/36/8/307

[20] Vagin, N. P., Ionin, A. A., Klimachev, Yu. M., Kochetov, I. V., Napartovich, A. P., Sinitsyn, D. V., and Yuryshev, N. N., "Glow Discharge in Singlet Oxygen," *Plasma Physics Reports*, Vol. 29, No. 3, 2003, pp. 211–219. doi:10.1134/1.1561115

[21] Vasiljeva, A. N., Klopovskiy, K. S., Kovalev, A. S., Lopaev, D. V., Mankelevich, Y. A., Popov, N. A., Rakhimov, A. T., and Rakhimova, T. V., "On the Possibility of $O_2(a1\Delta)$ Production by a Non-Self-Sustained Discharge for Oxygen–Iodine Laser Pumping," *Journal of Physics D: Applied Physics*, Vol. 37, No. 17, 2004, pp. 2455–2468. doi:10.1088/0022-3727/37/17/019

[22] Carroll, D. L., Verdeyen, J. T., King, D. M., Zimmerman, J. W., Laystrom, J. K., Woodard, B. S., Richardson, N., Kittell, K., Kushner, M. J., and Solomon, W. C., "Measurement of Positive Gain on the 1315 nm Transition of Atomic Iodine Pumped by $O_2(a1\Delta)$ Produced in an Electric Discharge," *Applied Physics Letters*, Vol. 85, No. 8, 2004, pp. 1320–1322. doi:10.1063/1.1784519

[23] Carroll, D. L., Verdeyen, J. T., King, D. M., Zimmerman, J. W., Laystrom, J. K., Woodard, B. S., Benavides, G. F., Kittell, K. W., and Solomon, W. C., "Path to the Measurement of Positive Gain on the 1315-nm Transition of Atomic Iodine Pumped by $O2(a^1\Delta)$ Produced in an Electric Discharge," *IEEE Journal of Quantum Electronics*, Vol. 41, No. 2, 2005, pp. 213–223. doi:10.1109/JQE.2004.839691

[24] Rawlins, W. T., Lee, S., Kessler, W. J., and Davis, S. J., "Observations of Gain on the $I(^2P_{1/2} \rightarrow {}^2P_{3/2})$ Transition by Energy Transfer from $O_2(a^1\Delta g)$ Generated by a Microwave Discharge in a Subsonic-Flow

Reactor," *Applied Physics Letters*, Vol. 86, No. 5, 2005, p. 051105. doi:10.1063/1.1861503

[25] Carroll, D. L., Verdeyen, J. T., King, D. M., Zimmerman, J. W., Laystrom, J. K., Woodard, B. S., Benavides, G. F., Kittell, K., Stafford, D. S., Kushner, M. J., and Solomon, W. C., "Continuous-Wave Laser Oscillation on the 1315 nm Transition of Atomic Iodine Pumped by $O_2(a^1\Delta g)$ Produced in an Electric Discharge," *Applied Physics Letters*, Vol. 86, No. 11, 2005, p. 111104. doi:10.1063/1.1883317

[26] King, D. M., Carroll, D. L., Verdeyen, J. T., Laystrom, J. K., Benavides, G. F., Palla, A. D., Zimmerman, J. W., Woodard, B. S., and Solomon, W. C., "Power Enhancement of the Hybrid ElectricOIL Laser," *37th AIAA Plasmadynamics and Lasers Conference*, AIAA Paper 2006-3756, 2006.

[27] Braginskiy, O. V., Vasilieva, A. N., Klopovskiy, K. S., Kovalev, A. S., Lopaev, D. V., Proshina, O. V., Rakhimova, T. V., and Rakhimov, A. T., "Singlet Oxygen Generation in O_2 Flow Excited by RF Discharge: I. Homogeneous Discharge Mode: α-Mode," *Journal of Physics D: Applied Physics*, Vol. 38, No. 19, 2005, pp. 3609–3625. doi:10.1088/0022-3727/38/19/010

[28] Hicks, A., Norberg, S., Shawcross, P., Lempert, W. R., Rich, J. W., and Adamovich, I. V., "Singlet Oxygen Generation in a High Pressure Non-Self-Sustained Electric Discharge," *Journal of Physics D: Applied Physics*, Vol. 38, No. 20, 2005, pp. 3812–3824. doi:10.1088/0022-3727/38/20/007

[29] Hicks, A., Tirupathi, S., Utkin, Yu., Jiang, N., Lempert, W. R., Rich, J. W., Adamovich, I. V., Galbally-Kinney, K., Kessler, W. J., Rawlins, W. T., Mulhall, P. A., and Davis, S. J., "Gain Measurements in a Non-Self-Sustained Electric Discharge Pumped Oxygen-Iodine Laser Cavity," *37th AIAA Plasmadynamics and Lasers Conference*, AIAA Paper 2006-3754, 2006.

[30] Hicks, A., Utkin, Yu. G., Lempert, W. R., Rich, J. W., and Adamovich, I. V., "Continuous Wave Operation of a Non-Self-Sustained Electric Discharge Pumped Oxygen-Iodine Laser," *Applied Physics Letters*, Vol. 89, No. 24, 2006, p. 241131. doi:10.1063/1.2408668

[31] Raizer, Yu. P., *Gas Discharge Physics*, Springer–Verlag, Berlin, 1991.

[32] McLeary, R. and Gibbs, W. E. K., "CW CO_2 Laser at Atmospheric Pressure," *IEEE Journal of Quantum Electronics*, Vol. 9, No. 8, 1973, pp. 828–833. doi:10.1109/JQE.1973.1077743

[33] Rich, J. W., Bergman, R. C., and Lordi, J. A., "Carbon Monoxide Laser Systems," U.S. Air Force Avionics Labs, Wright–Patterson AFB TR AFAL-TR-78-37, 1978.

[34] Basov, N. G., Babaev, I. K., Danilychev, V. A., Mikhailov, M. D., Orlov, V. K., Savelev, V. V., Son, V. G., and Cheburkin, N. V., "Closed Cycle CW CO_2 Laser Employing an Electron Beam Ionizer," *Soviet Journal of Quantum Electronics*, Vol. 6, No. 4, 1979, pp. 772–781.

[35] Kovalev, A. S., Muratov, E. A., Ozerenko, A. A., Rakhimov, A. T., and Suetin, N. V., "Structure of a Beam-Driven RF Discharge in a Gas Flow," *Soviet Journal of Plasma Physics*, Vol. 11, No. 7, 1985, pp. 515–519.

[36] Napartovich, A. P., "Physics of High-Power CO Laser," "*Gas Lasers: Recent Developments and Future Prospects*," edited by W. J. Witteman, and V. N. Ochkin, NATO ASI Series, Springer, New York, 1996, pp. 11–22.

[37] Hill, A. E., "Continuous Uniform Excitation of Medium-Pressure CO_2 Laser Plasmas by Means of Controlled Avalanche Ionization," *Applied Physics Letters*, Vol. 22, No. 12, 1973, p. 670. doi:10.1063/1.1654548

[38] Generalov, N. A., Zimakov, V. P., Kosynkin, V. D., Raizer, Yu. P., and Roitenburg, D. I., "Method for Significantly Increasing the Stability Limit of the Discharge in Fast-Flow Large-Volume Lasers," *Technical Physics Letters*, Vol. 1, No. 5, 1975, p. 201.

[39] Matzing, H., "Chemical Kinetics of Flue Gas Cleaning by Irradiation by Electrons," *Advances in Chemical Physics*, edited by I. Prigogine, and S. A. Rice, Vol. 80, Wiley, New York, 1991, pp. 315–403.

[40] Macheret, S. O., Shneider, M. N., and Miles, R. B., "Modeling of Air Plasma Generation by Electron Beams and High-Voltage Pulses," *31st AIAA Plasmadynamics and Lasers Conference*, AIAA Paper 2000-2569, 2000.

[41] Macheret, S. O., Shneider, M. N., and Miles, R. B., "Modeling of Plasma Generation in Repetitive Ultra-Short DC, Microwave, and Laser Pulses," *32nd AIAA Plasmadynamics and Lasers Conference and 4th Weakly Ionized Gases Workshop*, AIAA Paper 2001-2940, 2001.

[42] Macheret, S. O., Shneider, M. N., and Miles, R. B., "Modeling of Air Plasma Generation by Repetitive High-Voltage Nanosecond Pulses," *IEEE Transactions on Plasma Science*, Vol. 30, No. 3, 2002, pp. 1301–1314. doi:10.1109/TPS.2002.802142

[43] Macheret, S. O., Shneider, M. N., and Murray, R. C., "Ionization in Strong Electric Fields and Dynamics of Nanosecond-Pulse Plasmas," *Physics of Plasmas*, Vol. 13, No. 2, 2006, p. 023502. doi:10.1063/1.2172926

[44] Palm, P., Ploenjes, E., Adamovich, I., and Rich, J., "Mitigation of Electron Attachment and Recombination in Atmospheric Pressure Air Plasmas," *33rd Plasmadynamics and Lasers Conference*, AIAA Paper 2002-2224, 2002.

[45] Lee, W., Frederickson, K., Palm, P., Adamovich, I., Rich, J. W., and Lempert, W., "Mitigation of Oxygen Attachment in High Pressure Air Plasmas by Vibrational Excitation," *35th Plasmadynamics and Lasers Conference*, AIAA Paper 2004-2257, 2004.

[46] Kruger, C. H., Laux, C. O., Yu, L., Packan, D. M., and Pierrot, L., "Nonequilibrium Discharges in Air and Nitrogen Plasmas at Atmospheric Pressure," *Pure and Applied Chemistry*, Vol. 74, No. 3, 2002, pp. 337–347. doi:10.1351/pac200274030337

[47] Cobine, J. D., *Gaseous Conductors: Theory and Engineering Applications*, Dover, New York, 1958.

[48] Salyer, T. R., Collicott, S. H., and Schneider, S. P., "Feedback Stabilized Laser Differential Interferometry for Supersonic Blunt Body Receptivity Experiments," *38th AIAA Aerospace Sciences Meeting and Exhibit*, AIAA Paper 2000-0846, 2000.

[49] Gordiets, B. F., Osipov, V. A., and Shelepin, L. A., *Kinetic Processes in Gases and Molecular Lasers*, Gordon and Breach, London, 1988.

[50] Heylen, A. E. D., "Electrical Ionization and Breakdown of Gases in a Crossed Magnetic Field," *Proceedings of the Institution of Electrical Engineers*, Vol. 127, Pt. A, 1980, p. 221.

[51] Dargan, C. L., and Heylen, A. E. D., "Uniform-Field Sparking Voltages of Gases in Crossed Magnetic Fields," *Proceedings of the Institution of Electrical Engineers*, Vol. 115, No. 7, 1968, p. 1034.

[52] Sutton, G. W., and Sherman, A., *Engineering Magnetohydrodynamics*, McGraw–Hill, New York, 1965.

[53] Adamovich, I. V., Rich, J. W., and Nelson, G. L., "Feasibility Study of Magneto-Hydrodynamics Acceleration of Unseeded and Seeded Air Flows," *AIAA Journal*, Vol. 36, No. 4, 1998, pp. 590–597. doi:10.2514/2.410

[54] Chou, M.-S., and Zukowski, T. J., "Ignition of $H_2/O_2/NH_3$, $H_2/Air/NH_3$, and $CH_4/O_2/NH_3$ Mixtures by Excimer-Laser Photolysis of NH_3," *Combustion and Flame*, Vol. 87, No. 2, 1991, pp. 191–202. doi:10.1016/0010-2180(91)90169-C

[55] Lavid, M., Nachson, Y., Gulati, S. K., and Stevens, J. G., "Photochemical Ignition of Premixed Hydrogen/Oxygen Mixtures with ArF Laser," *Combustion Science and Technology*, Vol. 96, No. 4, 1994, p. 231. doi:10.1080/00102209408935357

[56] Roux, F., Michaud, F., and Vervloet, M., "High Resolution Fourier Spectrometry of $^{14}N_2$ Violet Emission Spectrum: Extensive Analysis of the $C3\Pi_u - B3\Pi_g$ System," *Journal of Molecular Spectroscopy*, Vol. 158, No. 2, 1993, pp. 270–277. doi:10.1006/jmsp.1993.1071

[57] Kovacs, I., *Rotational Structure in the Spectra of Diatomic Molecules*, Elsevier, New York, 1969.

[58] Belikov, A. E., Sharafutdinov, R. G., and Strekalov, M. L., "Temperature Dependence of the Rotational Relaxation Time in Nitrogen," *Chemical Physics Letters*, Vol. 231, Nos. 4–6, 1994, pp. 444–448. doi:10.1016/0009-2614(94)01269-5

[59] Adamovich, I., Bao, A., Lou, G., Nishihara, M., Rich, J. W., and Lempert, W., "Fuel Oxidation and Ignition in Premixed Hydrocarbon-Air Flows by Nonequilibrium Plasmas," *59th Gaseous Electronics Conference*, American Physical Society, 2006.

[60] Davis, S. J., and Hanko, L., "An I_2 Flow Rate Diagnostic for the Oxygen Iodine Laser," *Laser Digest*, Air Force Weapons Lab., Kirtland AFB, AFWL-TR-79-104, 1979.

[61] Davis, S. J., Kessler, W. J., and Bachmann, M., "Collisional Broadening of Absorption Lines in Water Vapor and Atomic Iodine Relevant to COIL Diagnostics," *Proceedings of SPIE 3268*, International Society for Optical Engineering, Paper 80, 1999.

[62] Davis, S. J., Kessler, W. J., and Keating, P. K., "Progress in the Development of Sensors for COIL Devices," *Proceedings of SPIE 3931*, International Society for Optical Engineering, Paper 24, 2000.

[63] Newman, S. M., Lane, I. C., Orr-Ewing, A. J., Newnham, D. A., and Ballard, J., "Integrated Absorption Intensity and Einstein Coefficients for the $O_2(a^1\Delta_g \rightarrow X^3\Sigma_g^-)$ (0,0) Transition: A Comparison of Cavity Ringdown and High Resolution Fourier Transform Spectroscopy with a Long-Path Absorption Cell," *Journal of Chemical Physics*, Vol. 110,

No. 22, 1999, p. 10749.
doi:10.1063/1.479018

[64] Lafferty, J., Solodov, A. M., Lugez, C. L., and Fraser, G. T., "Rotational Line Strength and Self-Pressure-Broadening Coefficients for the 1.27 μm $a^1\Delta_g \rightarrow X^3\Sigma_g^- v = 0 \rightarrow 0$ band of O_2," *Applied Optics*, Vol. 37, No. 12, 1998, p. 2264.
doi:10.1364/AO.37.002264

[65] Babcock, H. D., and Herzberg, L., "Fine Structure of the Red System of Atmospheric Oxygen Bands," *Astrophysical Journal*, Vol. 108, Sept. 1948, pp. 167–190.
doi:10.1086/145062

[66] Watson, J. K. G., "Rotational Line Intensities in $^3\Sigma - {}^1\Sigma$ Electronic Transitions," *Canadian Journal of Physics*, Vol. 46, No. 14, 1968, pp. 1637–1643.

S. Macheret
Associate Editor